Integrated Antennas for Efficient and Directional Coupling to Plasmonic Waveguides

by

Aziz Karaşahin

A Thesis Submitted to the

Graduate School of Engineering

in Partial Fulfillment of the Requirements for

the Degree of

Master of Science

in

Electrical & Electronics Engineering

Koç University

August, 2015

Koç University

Graduate School of Sciences and Engineering

This is to certify that I have examined this copy of a master's thesis by

Aziz Karaşahin

and have found that it is complete and satisfactory in all respects,
and that any and all revisions required by the final
examining committee have been made.

Committee Members:

Asst. Prof. Şükrü Ekin Kocabaş (Advisor)

Assoc. Prof. Kaan Güven

Asst. Prof. Alexandr Jonas

Date: _____

To my parents and sister...

Acknowledgments

The blind decision that I made to come to Koç University two years ago, resulted in great personal academic gratification and many lovely friendships. Without doubt, none of these would be possible without guidance and toleration of my advisor Prof. Şükrü Ekin Kocabaş. I would to like express my deepest appreciation to him for his invaluable role that he played in relation to both academic and personal life. He is not only a professional academics but also a humble friend. Whenever I got stuck at any step in my research, his stimulating questions and logical approaches always facilitated my progress. Whenever I needed help due to personal issues he always behaved as a friend with positive attitude. I felt very privileged to work with him.

For the fabrication side of my studies, I owe many thanks to Dr. Cenk Yanık from Sabancı University Nanotechnology Research Center (SUNUM) who shared his knowledge and experienced fabrication tricks. He helped a lot in the e-beam lithography steps. Dr. Barış Yağcı and Cansu Yıldırım from Koç University Surface Science and Technology Center (KUYTAM) were always kind and helpful, whenever I failed to have good quality SEM images, I found them helping me with enthusiasm. I am also very grateful to Ümmü Koç who gave me training to use Koç University Cleanroom. I also thank Dr. Özgür Birer for allowing his time to teach me how to use thermal evaporation system.

I used computer cluster of Koç University for some of my simulations. Hüseyin Özbey quickly solved technical problems which I faced, and he was always accessible via phone and e-mails. I appreciate his great efforts that made my progress faster and easier.

I am also grateful to Prof. Kaan Güven and Prof. Alexandr Jonas for being in my

thesis committee and for their valuable feedbacks. I acknowledge Prof. Deniz D. Yavuz and Prof. Tekin Dereli who always motivated me for future academic studies with their guidance and support.

My special thanks are for M. Haroon Qureshi who supported me with his brilliant knowledge and priceless help on language aspects. He was not only a sociable friend but also great teacher that answers my countless questions in broad topics with patience.

Friends are indispensable part of graduate studies. I had many of them who altogether made graduate studies fantastic experience for me. I would like to express my appreciation to following friends and colleagues: Berkay Yılmaz, Muhammad Zakwan, Yasin Karadağ, Hüseyin İnan, Yunus Emre Kesim, Sami Bolat, Amir Ghobadi, M. Maiz Ghauri, Vahid Pourreza Goushchi, İsmail Yorulmaz, H. Serhat Tetikol, Mustafa Eryürek, Adeel Afridi and Ongun Arısev.

I want to also extend my thanks to Pakistani community of Koç University. They were all kind, welcoming and warm friends that I spent great time with. I found a great opportunity to know their fantastic culture and to taste their delicious cuisine.

I want to also acknowledge my first science teacher Mustafa Topkara, who placed foundation stone of my science career and opened my long way to understand the universe with the light of science.

The staff of Graduate School of Science and Engineering namely Emine Büyükdurmuş, Elif Tüysüz and Gözde Şirin were heroes behind the curtain that built connections between graduate students and administration. I appreciate their great effort that simplified complicated administrative formalities.

I want to acknowledge support from TUBİTAK-BİDEB national MS Scholarship Program and TUBİTAK Project No: 112E247 for providing funding resources on this work.

It is very hard to find appropriate words to express my deepest thanks for my lovely

family. Last but not the least, I want to thank my parents and sister, they always trusted in me and supported me in my decisions. They always approached me politely and with understanding and never let their love down.

ABSTRACT

The use of metallic nano structures as building blocks of future optical integrated circuits is an appealing idea, since such an approach combines several advantages such as sub-wavelength field confinement, guided wave propagation and extraordinary field intensities. In fact, these are key requirements for designing optical integrated circuits which can process information at optical bandwidths, much higher than today's electronic circuits.

Plasmonic waveguides are fundamental components of plasmonic circuits which can potentially be used to transfer data between different parts on an optical chip. One of the open problems in the field is to efficiently couple the light from free space to these waveguides or from a waveguide mode to free space. Previous studies introduced scatterers which are placed at the opening of waveguides as couplers, however they lack analytical design formalism and have no systematic control over radiation angle.

This dissertation focuses on designing efficient couplers for plasmonic waveguides by employing more analytical approaches. We begin with a brief review of electromagnetic theory before introducing mode properties of plasmonic slot waveguides. Then, we investigate scattering characteristics of various scatterer designs. In the modeling chapter, we illustrate how to model an array of antenna scatterers embedded in waveguides for efficient and directional coupling by employing scattering matrix formalism and antenna arrays. In the last part of the dissertation, we show fabrication details of plasmonic structures and we present the schematic of the optical measurement setup. Finally, we present conclusions and future directions of this research.

ÖZETÇE

Geleceğin bütünleşik optik devreleri için metal nano yapıların kullanılması fikrini cazip kılan nedenler arasında bu tarz yaklaşımların elektromanyetik alanları dalga boyundan daha küçük boyutlara yoğunlaştırabilmesi, kılavuzlanmış dalga iletimine imkan vermesi ve olağandışı yükseklikte alan yoğunluklarının elde edilebilmesi sayılabilir.

Plazmonik dalga kılavuzları optik yongalar üzerinde veri iletiminde kullanılabilecek plazmonik devrelerin temel elemanlarını oluşturmaktadır. Bu konudaki ucu açık problemlerden biri de bu dalga kılavuzlarına dışardan ışığı eşleştirmek ya da dalga kılavuzu kipindeki enerjiyi dışarıya verimli şekilde aktarabilmektir. Plazmonik dalga kılavuzlarının sonundaki açıklıklara konumlandırılan saçıcıları eşleştirici olarak kullanan çalışmalar mevcut olsa da bu çalışmalar analitik tasarım süreçlerinden yoksun ve dışarıya çıkan radyasyon açısı üzerinde direkt kontrole sahip değillerdir.

Bu tez, daha analitik yaklaşımlar kullanarak plazmonik dalga kılavuzlarına verimli eşleştiricilerin tasarımı üzerine yoğunlaşmaktadır. Biz plazmonik yivli dalga kılavuzlarının kip özelliklerini incelemeden önce elektromanyetik teorinin kısa bir özeti ile başlıyoruz. Daha sonra farklı saçıcı tasarımlarının saçıcılık karakteristiklerini inceliyoruz. Modelleme bölümünde ise dalga kılavuzuna gömülü sıralı antenlerin verimli ve yön bağımlı saçıcılar olarak kullanılmasına imkan verecek şekilde modellemesini S-matris ve sıralı antenler formalizmlerini kullanarak gösteriyoruz. Tezin son bölümünde ise bu tarz plazmonik yapıların üretimi hakkındaki detayları paylaşıp, tasarlanan optik ölçüm düzeneğini sunuyoruz. Son olarak da neticelerimizi paylaşıp, geleceğe yönelik araştırma yönleri hakkında yorumda bulunuyoruz.

Contents

List of Figures

Chapter 1

Introduction

Surely one of the greatest inventions of 20th century was the invention of transistor that ignited the computing revolution. Within a short time, after the development of integrated circuits, computers came into existence [1]. Since then, steady improvements of integrated circuits are enabled by doubling of transistor densities by shrinking their sizes every two years. Such an increase in computational power paved the way for wide range of technologies including personal computers, smart phones, medical imaging devices, satellites among others. In fact, the prediction regarding transistor densities was made fifty years ago by Moore but it seems that trend still continues to hold [2]. However, as transistors became smaller several challenging problems emerged such as increased power consumption and increased time-delays due to resistance and capacitance effects [3]. In fact, performance of future electronic circuits will be limited due to the reasons listed above, hence new solutions are needed to supply the increasing demand for computation power.

At the point where electronics get stuck, optical technologies, that employ photons instead of electrons, are emerging as an alternative. There are many ongoing efforts to design optical components such as transmitters, multiplexers and photo detectors integrated to electronics to employ them in optical data transmission [4,5]. Among these efforts, though it is in infancy, silicon photonics is one of the promising fields to increase data transmission speed between chips or within a chip. In fact, recently first silicon photonic link operating at 50 Gbit/s was announced by Intel [6]. The efforts relating

silicon photonics is not limited to interconnects, there are also many ongoing studies to implement integrated silicon photonics for future optical chips [7]. However, size of such optical components are comparable with their working wavelength, i.e. mostly in the order of micrometer. Hence, compared with the nanometer scale transistors, there is a huge size mismatch between electronics and photonics. This is one of the biggest challenges of optical devices since shrinking them is necessary to implement photonic integrated chips that surpass their counterparts in computational power.

Another emerging optical technology called plasmonics can offer some solutions to size mismatch problem of optical components. Surface plasmons that exists at dielectric-metal interfaces are simply electron oscillations which are coupled to photons. Although this phenomena has found many applications such as an infrared absorber [8], molecular sensors [9, 10] and in optofluidic channels [11], more breakthrough inventions can be achieved by using their sub-wavelength nature to manipulate photons. Since plasmons work in optical frequencies, they also come with the advantage of high bandwidth for faster communications. However, there are many challenging problems to be solved [12, 13] before implementing integrated optical chips. Those include design of plasmonic lasers, multiplexers, transistors, modulators, resonators and couplers. One of the fundamental class of components is waveguides. They are components that are used to transport the energy or data from one place to another place in the chip. In that sense, they are like roads of the chip that connect various components to each other. Until now, various plasmonic waveguides structures which promise high field confinements and moderate propagating lengths are experimentally demonstrated [14–17].

Integration of plasmonic waveguides to optical chips require a careful investigation. Although there are various studies that examine mode properties of such waveguides [18–20], coupling of light to the waveguide from air or coupling between waveguides are ongoing research areas that need to be studied. Until now, although some studies

introduced designs to couple light between dielectric waveguide and plasmonic waveguide, there are not much detailed results that show coupling between waveguide and an optical mode coming from the air side. The ones that exist in literature mainly focused on increasing light coupling by placing scatterers at the end of waveguides. However, these designs only consider geometries where couplers are located at the open end of waveguides, so scatterers interact with waveguide mode in a very limited region, i.e. only end of the waveguide. On the other hand, existing designs have no control over the angle of radiation that is coupled to the free space.

In this dissertation, we show increased coupling by placing an array of scatterers (antennas) to the middle of plasmonic two wire transmission line waveguide (TWTL). We also introduce semi-analytical modeling of arrayed couplers by using antenna array concepts taken from RF antenna theory. By using this approach, we also model the direction of radiated light from couplers.

We start the thesis by giving necessary tools such Maxwell's equations, electromagnetic properties of materials and plasmonic phenomena in Chapter 2. This chapter also aims to establish the notations to be used in later chapters.

In Chapter 3, we will demonstrate various plasmonic waveguide structures, their dispersion relations and mode properties. First, analytical calculation of dispersion relation of two dimensional waveguides will be introduced. Then, methods to find mode properties of three dimensional slot and transmission line waveguides by using finite-difference-time-domain (FDTD) will be shown. Finally, after setting up the method, the effect of geometry and substrate on dispersion relations will be investigated.

Chapter 4 will begin with some examples of antenna couplers that exist in literature. Later, we will introduce an antenna coupler design for slot waveguides with 50 nm gap. After that, radiation strengths and scattering characteristics of various individual

scatterers which are placed at the middle of transmission line waveguides will be studied.

After finding parameters of resonant antenna in desired wavelength, Chapter 5 will be about modeling of these scatterers. First, methods to find S-parameters of antenna scatterers will be explained. Then, transmission and reflection results of arrayed antenna scatterers to compare FDTD simulations and our model will be shown. Later, by finding excitation amplitudes of array elements using an S-matrix approach, antennas will be modeled as arrays by using concepts adopted from RF antennas. Lastly, radiation properties predicted by the S-matrix model will be compared with FDTD simulation results.

Fabrication methods used, steps followed, problems encountered, and solutions proposed will be explained in the Chapter 6. SEM images of fabricated structures will be shown. Moreover, the schematic of optical setup will be shared. Lastly, we will lay out the conclusion and future directions.

Chapter 2

Background Information

Electromagnetics, as a fundamental field in physics and electrical engineering, describes the behavior electric charges at rest or in motion (electric currents) and their interaction with electromagnetic waves which can freely propagate in free space. Modern electromagnetic theory was born with breakthrough experiments carried out by Gauss, Ampere, Lorentz and Faraday in the 19th century. It became a unified field thanks to James Clark Maxwell who systematized previous experimental findings into a well recognized set of equations. This exciting field has attracted a lot of attention in the 20th century and has given rise to technologies such as wireless communications, antennas, radar, circuit theory, optical communications and modern electronics.

While rigorous discussion of Maxwell's equations and their implications have been discussed in many textbooks of electrodynamics and electrical engineering [21–23], this chapter introduces a simple review of necessary background in electromagnetics and plasmonics which will comprise the body of this thesis.

2.1 Maxwell's Equations

Classical macroscopic Maxwell's Equations are accurate enough to model behavior of dielectric and metallic materials, even down to nanoscale.

The Maxwell's Equations in SI units may be written as

$$\nabla \times \mathbf{E} = -\frac{\partial \mathbf{B}}{\partial t}, \tag{2.1}$$

$$\nabla \times \mathbf{H} = \mathbf{J_s} + \frac{\partial \mathbf{D}}{\partial t}, \tag{2.2}$$

$$\nabla \cdot \mathbf{D} = \rho_s, \tag{2.3}$$

$$\nabla \cdot \mathbf{B} = 0, \tag{2.4}$$

where $\mathbf{E}$ is the electric field in (Volts/m), is the magnetic field in (Amperes/m), $\mathbf{D}$ is the electric displacement in (Coulomb/m^2) and $\mathbf{B}$ is the magnetic flux density in (Tesla). Here we use boldface letters to show vectorial quantities. Equation 2.4 shows that divergence of $\mathbf{B}$ is 0 that means no magnetic charges exist as source. Subscript s is used when writing source terms of charge ($\rho_\mathbf{s}$) and current ($\mathbf{J_s}$). They are called free source terms which represent the stimuli given to the system. The relations between electric field and electric displacement; magnetic field and magnetic flux density are called constitutive relations and they are written as Equation 2.5 and Equation 2.6, respectively.

$$\mathbf{D} = \epsilon_0 \mathbf{E} + \mathbf{P}, \tag{2.5}$$

$$\mathbf{B} = \mu_0(\mathbf{H} + \mathbf{M}), \tag{2.6}$$

where $\mathbf{P}$ represents electric polarization and $\mathbf{M}$ represents magnetization which are defined as average electric and magnetic dipole moments per unit volume, respectively. ϵ_0 is called vacuum permittivity and μ_0 is called vacuum permeability. Equation 2.5

and Equation 2.6 can also be written as

$$\mathbf{D} = \epsilon \mathbf{E}, \tag{2.7}$$

$$\mathbf{B} = \mu \mathbf{H}, \tag{2.8}$$

by including polarization and magnetization effects in the permittivity and permeability terms. Those new terms ϵ and μ are different than free space values and their relation are given as

$$\epsilon = \epsilon_0 \epsilon_r, \tag{2.9}$$

$$\mu = \mu_0 \mu_r, \tag{2.10}$$

where ϵ_r and μ_r are called relative permeability and relative permeability, respectively. Constitutive relations Equations 2.5-2.6 can be further expanded to explicitly show effects of medium as

$$\mathbf{M} = \chi_m \mathbf{H}, \tag{2.11}$$

$$\mathbf{P} = \epsilon_0 \chi \mathbf{E}. \tag{2.12}$$

Here $\mathbf{E}$ and $\mathbf{H}$ are total fields that includes both effects of material and source. Magnetic susceptibility (χ_m) and electric susceptibility (χ) are material-dependent constants that define the response of material to the electromagnetic waves. These coefficients are assumed to be constant scalars which is the attribute of isotropic medium of which material properties do not depend on the direction. It is also assumed that coefficients are independent of position (homogeneous medium) and field intensities (linear medium). Though these equations can be modified for non-simple medium, it is not the scope of this thesis, and we forward the interested reader to the more advanced text books [21].

Most of the medium we encounter are non-magnetic in nature which means they do not have magnetization ($\mathbf{M}$), so $\mu = \mu_0$ for such materials. Throughout the rest of the this text, we will be using non-magnetic medium and permeability assumption will be held. Properties of materials will be solely dependent on their permittivity. The relation between permittivity and susceptibility is found by inserting 2.12 to 2.5 and using 2.9 which results in $\epsilon_r = 1 + \chi$.

2.2 Electromagnetic Properties of Metals

In this section we will derive the relations that explain the electromagnetic properties of materials, particularly metals. First, we will give the relation between permittivity and conductivity. Later, we will introduce the another set of constants that is commonly employed to study optical materials.[3]

One way of expressing current density is using Ohm's Law which is shown below

$$\mathbf{J} = \sigma \mathbf{E} \tag{2.13}$$

where σ is defined as conductivity. The relation between current density ($\mathbf{J}$) and polarization ($\mathbf{P}$) can be written by using charge conservation relation ($\nabla \cdot \mathbf{J} = -\frac{\partial \rho}{\partial t}$) as

$$\mathbf{J} = \frac{\partial \mathbf{P}}{\partial t}. \tag{2.14}$$

The relation between ϵ and σ is found by correcting the previous assumption which we made to write 2.7 and 2.8 where we assumed that fields behave locally in time. However, in most of the medium, permittivity depends on frequency which yields that fields are not local in time. Detailed mathematical derivation of this effect can be done by taking

[3]Optical frequencies span visible region of electromagnetic spectrum.

Fourier Transform of 2.7 and 2.8 [24]. By taking into account spatial and temporal dispersion, frequency dependent 2.7 and 2.13 relations are written as

$$\mathbf{D}(\mathbf{K},\omega) = \epsilon_0 \epsilon_r(\mathbf{K},\omega)\mathbf{E}(\mathbf{K},\omega) \tag{2.15}$$

$$\mathbf{J}(\mathbf{K},\omega) = \sigma(\mathbf{K},\omega)\mathbf{E}(\mathbf{K},\omega) \tag{2.16}$$

Using 2.15, 2.16, 2.5 and 2.14 we end up with relation between relative permittivity and conductivity as

$$\epsilon_r(\mathbf{K},\omega) = 1 + \frac{i\sigma(\mathbf{K},\omega)}{\epsilon_0 \omega} \tag{2.17}$$

where $\epsilon_r = \epsilon_1 + i\epsilon_2$ and $\sigma = \sigma_1 + i\sigma_2$ are complex quantities. As seen in Equation 2.17, those two quantities are not independent and can be used to define material properties interchangeably. Although permitivity and conductivity are enough to calculate absorption and scattering cross sections, here we will define another set of parameters called complex refractive index $n(\omega) = n_r + i\kappa(\omega)$ which gives direct information regarding wave propagation such as phase accumulation or attenuation. The intimate relation between permittivity and refractive index is given by $n(\omega) = \sqrt{\epsilon(\omega)}$. By employing complex algebra following relations are written.

$$\epsilon_1 = n^2 - \kappa^2 \tag{2.18a}$$

$$\epsilon_2 = 2n\kappa \tag{2.18b}$$

The preference between using complex refractive index or complex permittivity depends on the application. For instance, for the optical frequencies, a common method uses

reflection and transmission measurements to determine directly complex refractive index of materials [25].

2.2.1 Lorentz and Drude Model

Material properties, described by complex refractive index or complex permittivity, are directly responsible for matter-wave interactions and propagation of electromagnetic waves in the medium. The crucial question to be answered is how to model such properties to better understand interactions and even to engineer artificial materials with desired properties [26]. This question is simply answered for dielectric materials by H.A Lorentz by treating electrons as classical oscillators that oscillate under the effect of external electric field. Although this model uses only classical physics without considering any quantum mechanical effects, it is successful enough to explain experimental data.

The Lorentz model assumes that material is composed of identical, independent and isotropic (direction independent) charged particles of mass m and charge e. They oscillate with driving electric field acted on Lorentz force $\mathbf{F} = e\mathbf{E}$. They also feel the restoring force $K\mathbf{r}$ and damping force $b\dot{\mathbf{r}}$. The second order differential equation that governs this oscillatory movement is given by

$$m\ddot{\mathbf{r}} + b\dot{\mathbf{r}} + K\mathbf{r} = q\mathbf{E} \tag{2.19}$$

For the time harmonic fields which are oscillating with angular frequency ω, by using $e^{-j\omega t}$ convention (which will be followed in the rest of the thesis), displacement vector is written as

$$\mathbf{r} = \frac{(e/m)\mathbf{E}}{\omega_0^2 - \omega^2 - j\omega\gamma} \tag{2.20}$$

where $\omega_0^2 = K/m$,$\gamma = b/m$, e is the electric charge and m is effective mass of elec-

tron. Effective mass of electron is not the same with the rest mass and it depends on band structure of material [27]. Hence, effective mass values have to be taken into consideration for numerical calculations.

The displacements of charges from equilibrium position yields net dipole moment for each electron given by $\mathbf{p} = e\mathbf{r}$. Since we assumed that all particles are the identical, multiplying $\mathbf{p}$ with number of particles per volume (N) will yield polarization ($\mathbf{P}$) which is defined as net dipole moment per volume.

$$\mathbf{P} = \frac{(e^2 N/m)\mathbf{E}}{\omega_0^2 - \omega^2 - j\omega\gamma} \tag{2.21}$$

Here we define a new constant called plasma frequency $\omega_p^2 = Ne^2/m\epsilon_0$ which is a material dependent characteristic constant. By using the 2.21, 2.5, 2.7, real and imaginary parts of relative permittivity are written as

$$\epsilon_1 = 1 + \frac{\omega_p^2(\omega_0^2 - \omega^2)}{(\omega_0^2 - \omega^2)^2 + \omega^2\gamma^2} \tag{2.22}$$

$$\epsilon_2 = \frac{\omega_p^2\omega\gamma}{(\omega_0^2 - \omega^2)^2 + \omega^2\gamma^2} \tag{2.23}$$

Figure 2.1 shows a *Lorentzian* shape distribution of real and imaginary parts of relative permittivity. In this example (where $\omega_0 = 1.63eV$), imaginary part of permittivity reaches maximum value around $\omega \approx \omega_0$ and its maximum value is inversely proportional to γ. For lower($\omega << \omega_0$) and higher($\omega >> \omega_0$) frequencies, ϵ_2 goes to zero which indicates that oscillators are in phase with driving electric field. On the other hand, around $\omega \approx \omega_0$ the phase of permittivity change drastically which causes anomalous dispersion in the vicinity of ω_0.

Although simple Lorentz oscillator model can predict permittivities of broad class of

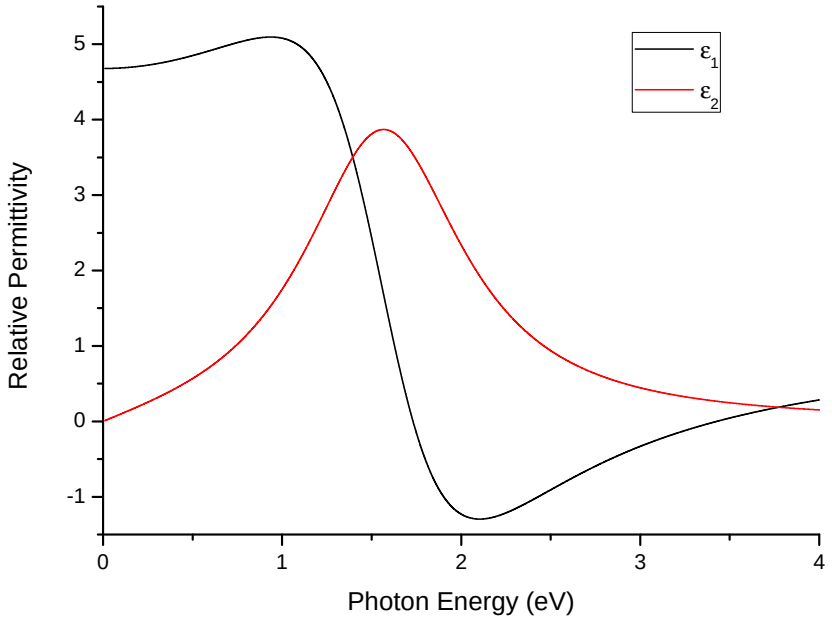

Figure 2.1: Lorentzian shape permittivity for parameters $\omega_p = 4.58eV$, $\omega_0 = 1.63eV$ and $\gamma = 0.71eV$.

materials, it can be further modified to include secondary effects such as lattice vibrations or can be reformulated for anisotropic materials as well. However, we will be working with metals in the rest of the thesis, which is why we will be able to simplify the Lorentz model for the metals. Metals do not possess a band gap as semiconductors or insulators, hence electrons of metals can be easily excited with very low energies. Therefore, they will be treated as free electrons by taking spring constant K in the Lorentz model as zero. Therefore, for metals, 2.22 and 2.23 can be written as

$$\epsilon_1 = 1 - \frac{\omega_p^2}{\omega^2 + \gamma^2} \tag{2.24}$$

$$\epsilon_2 = \frac{\omega_p^2 \gamma}{\omega(\omega^2 + \gamma^2)} \tag{2.25}$$

This simplified model is called as Drude model. Equations 2.24 and 2.25 can be investigated in three different regions. For the microwave frequencies ($\omega << \gamma$), relative permittivity is an imaginary number which causes very low skin depth for the waves

impinging on it. In the higher frequencies ($\omega >> \omega_p$), permittivity becomes a positive real number and metals behave as dielectrics. For the optical and near infrared regime, where ω is comparable with γ and ω_p, permittivity becomes a complex number which allows waves to partially penetrate on it.

2.2.2 Realistic Materials

The Drude model is adequate enough to theoretically predict the general trend of permittivity with varying frequency. However, the assumptions made to derive relations 2.24 and 2.25 can be violated by various effects such as interband transitions, permanent dipole moments or nonlinear effects. For instance, for gold, interband transitions start to occur at near infrared regime which changes permittivity predictions of Drude model. Such variations might result in drastic changes in the dispersion relation of waveguides that employ plasmons. Therefore, experimental data should be taken into account to accurately model material properties for simulation studies. Fortunately, a number of experimental data exists in the literature for common metals such as gold, silver and titanium. [25, 28, 29]. In the FDTD simulations which will be discussed in further chapters, we used experimental permittivity values taken from the literature.

2.3 Plasmonics

Plasmons are quantized collective oscillations of free electron gas which can exist in metals or plasma. They oscillate with plasma frequency ω_p which is defined by effective mass of electrons and their density in the material. In this sense, they are regarded as quasi-particles of plasma oscillations. Metal-dielectric interfaces also host plasmons whose intensity is decaying away from the interface in the perpendicular direction whereas

they propagate along the direction of interface. These surface waves are called *surface plasmons*; in fact, they are nothing more than confined electron excitations at the interface. When external electromagnetic waves (photons) impinge on such interfaces, under special circumstances, photons can couple to surface plasmons and they are called *surface plasmon polariton(SPP)s*. In that sense, SPPs are special solutions of Maxwell's equations that require positive and negative permittivity interfaces. This requirement can be satisfied by dielectrics and metals in optical and infrared frequencies.

Scattering from sub-wavelength metallic structures might also result in surface excitations which have non-propagative nature. These excitations are called *localized surface plasmons* in the literature. Interestingly, the interaction of electromagnetic waves with such scatterers are able to produce very high field enhancements in the local spots which can be employed for various purposes such as gain enhancement in laser dyes [30, 31], enhanced Raman signal [32] or sensors [33–35].

Surface plasmon polaritons are also very promising in the field of integrative photonics due to their capability of combining propagative nature and sub-wavelength confinement. However, before unleashing their potential in future integrated optics, there are many challenging tasks to be completed such as development of waveguides, optical switches, modulators, demultiplexers, multiplexers and couplers. Design of such components require a systematic approach, so it is necessary to start with properties of plasmonic waveguides which are key elements for designing highly integrated optical circuits.

Chapter 3

Dispersion Relations and Mode Properties of Plasmonic Waveguides

Surface plasmons are well studied phenomena since 1967, when first Kliewer and Fuchs studied modes and dispersion characteristics of metallic slab modeled with free electron gas [36]. Later, dispersion relation of the multi layered metallic films were also investigated by using Drude model and including retardation effects [37]. More recent studies proposed various three dimensional structures that employ surface plasmons for practical waveguiding [38–40].

The reason for surface plasmons to take such enormous attention is their capability of confining light to the sub-wavelength dimensions and allowing long propagation lengths at the same time [13].

Dispersion relations and mode distributions of waveguides are needed to be known in detail to design plasmonic components such as multiplexers, demultiplexers, filters and couplers. Therefore this chapter gives a background on the mode characteristics of various plasmonic waveguides, before studying couplers for them.

3.1 2D Plasmonic Waveguides

Dispersion relation of two dimensional plasmonic waveguides can be solved for single and multiple interfaces. In this section, we derive dispersion relations for metal-

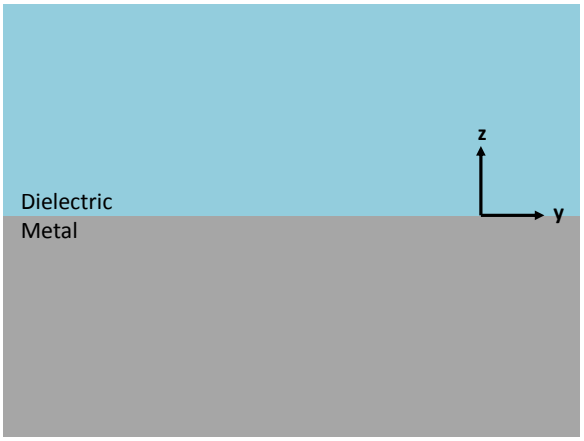

Figure 3.1: Geometry of IM Waveguide with single dielectric-metal interface.

insulator(IM), metal-insulator-metal (MIM) and insulator-metal-insulator (IMI) structures.

3.1.1 IM Waveguide

The most simple structure that can have confined plasmon modes are flat dielectric-metal interfaces. The figure 3.1 shows such an interface where plasma oscillations of electrons are confined at the interface and they evanescently decay in $+z$ and $-z$ directions. Here dielectric material is assumed to be lossless and metal permittivity is modeled with Drude model which is derived in 2.2.1. Therefore, in the desired frequency range, $\epsilon_1 > 0, \epsilon_2 = 0$ for the dielectric and $\epsilon_1 < 0, \epsilon_2 \neq 0$ for the metal.

The wave equation which is derived from Maxwell's Equations by using vector identity $\nabla \times (\nabla \times \mathbf{A}) = \nabla(\nabla \cdot \mathbf{A}) - \nabla^2 \mathbf{A}$ can be written for electric and magnetic fields as

$$\nabla^2 \mathbf{E} + \omega^2 \mu_0 \epsilon_0 \epsilon_r \mathbf{E} = 0 \tag{3.1}$$

$$\nabla^2 \mathbf{H} + \omega^2 \mu_0 \epsilon_0 \epsilon_r \mathbf{H} = 0 \tag{3.2}$$

For the mode propagating in y direction (with phase dependence $e^{j\beta y}$), $\frac{\partial}{\partial y}$ can be replaced by $j\beta$, and $\frac{\partial}{\partial x}$ can be replaced by 0 since there is no physical variance in x direction. By separating solutions into two sets as TM (only H_x, E_y, E_z are nonzero) and TE (only E_x, H_y, H_z are nonzero), one can write simplified wave equation for TM case as

$$\frac{\partial^2 H_x}{\partial z^2} + (k_0^2 \epsilon_r - \beta^2) H_x = 0 \tag{3.3}$$

and for TE case as

$$\frac{\partial^2 E_x}{\partial z^2} + (k_0^2 \epsilon_r - \beta^2) E_x = 0 \tag{3.4}$$

where $\epsilon_r = \epsilon_d$ in the dielectric and $\epsilon_r = \epsilon_m$ in the metal region. For TM solution of the guided mode, tangential component of H is continuous and it decays away from the interface. So, H_x is written as

$$H_x = H_{x0} e^{(j\beta y - j\omega t)} \begin{cases} e^{-\kappa_d z}, & \text{if } z > 0. \\ e^{\kappa_m z}, & \text{if } z < 0. \end{cases} \tag{3.5}$$

where $\beta^2 = k_0^2 \epsilon_r + \kappa_{d,m}^2$. Then, by using 2.2, E_y is written as

$$E_y = \frac{H_{x0} e^{(j\beta y - j\omega t)}}{j\omega\epsilon_0} \begin{cases} \frac{\kappa_d}{\epsilon_d} e^{-\kappa_d z}, & \text{if } z > 0. \\ \frac{-\kappa_m}{\epsilon_m} e^{\kappa_m z}, & \text{if } z < 0. \end{cases} \tag{3.6}$$

Continuity of E_y at the interface requires the following relation.

$$\frac{\kappa_d}{\kappa_m} = -\frac{\epsilon_d}{\epsilon_m} \tag{3.7}$$

Careful investigation of 3.7 shows that ϵ_d and ϵ_m must have opposite signs, and this is the case when ϵ_m takes negative values for metals at some frequency range. If the

equation 3.7 is solved for β by using above mentioned relation $\beta^2 = k_0^2\epsilon_r + \kappa_{d,m}^2$, one can easily get the following dispersion relation for the single interface.

$$\beta = k_0\sqrt{\frac{\epsilon_m\epsilon_d}{\epsilon_m + \epsilon_d}} \tag{3.8}$$

If the continuity of E_x and H_y fields are investigated for TE case by using the same approach, one can easily show that there is no allowed mode decaying away from interface for TE case. Therefore, it is concluded that, only TM modes are allowed to have confined mode at the interface.

Now, if we employ Drude model with negligible damping (2.24,2.25), 3.8 can be written as follows:

$$\beta = k_0\sqrt{\frac{(1 - \frac{\omega_p^2}{\omega^2})\epsilon_d}{(1 + \epsilon_d) - \frac{\omega_p^2}{\omega^2}}} \tag{3.9}$$

Figure 3.2 shows normalized $\omega - \beta$ diagram of a single interface which is calculated by using 3.8. For the frequencies in the vicinity of $\omega_p/\sqrt{(1 + n_d)}$, real and imaginary part of β increases drastically, hence surface plasmons exhibit large damping and increased confinement around this frequency. On the other hand, for the very low frequencies and very high frequencies, dispersion relation approaches to glass line.

3.1.2 Multiple Layer Waveguide

The idea to further confine the mode into smaller volume is using multiple layer structures which are composing of multiple dielectric-metal interfaces. Those structures are also in two dimension but they promise confining fields between layers. In fact, the

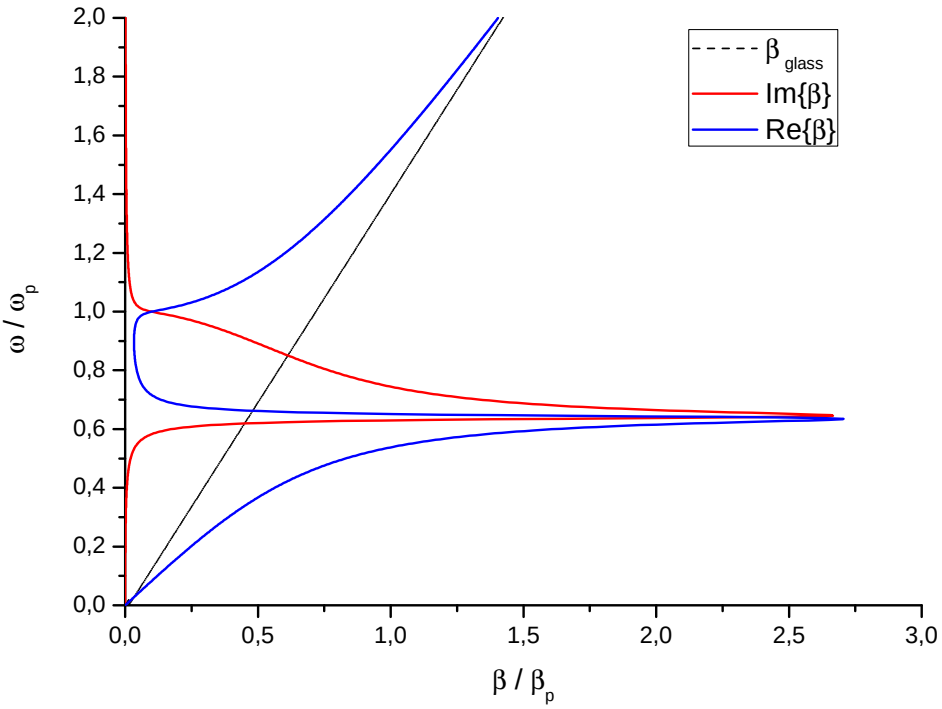

Figure 3.2: Normalized $\omega - \beta$ diagram for IM waveguide with glass (n=1.44) and $\gamma = 0.002\omega_p$. Black line is dispersion in glass, blue line is real part of wavenumber and red line represents imaginary part of wavenumber divided by $\beta_p = \omega_p/c_0$.

modes of such system are basically coupled modes of multiple interfaces. In order to understand the behavior of such coupled modes, we will solve the system of three alternating layers (metal-insulator-metal or insulator-metal-insulator) for the dispersion relations. This geometry has no variation x direction and mode is assumed to propagate in $+y$ direction. Middle layer has thickness d and system is symmetric in z direction. (Figure 3.3).

Although solution of multiple layer system requires a little bit more effort, exact same procedure will be applied to get the dispersion relation. We will start with TM modes as in the single interface case. Since we assumed that mode is confined in the gap, only fields which are exponentially decaying in the $+z$ for Layer 1 and in the $-z$ for Layer 3 will be considered. By keeping assumptions made for the phase variations in y and x

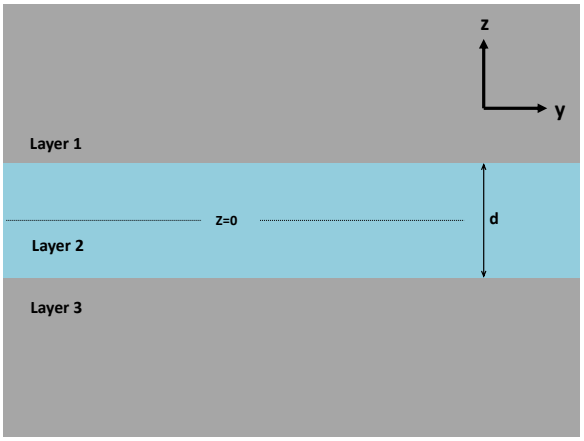

Figure 3.3: Geometry for multilayer plasmonic waveguide,i.e, metal-insulator-metal or insulator-metal-insulator interfaces.

directions, H_x can be written as

$$H_x = H_{x0}e^{(j\beta y - j\omega t)} \begin{cases} Ae^{-\kappa_1 z}, & \text{if } z > d/2 \\ Be^{\kappa_2 z} + Ce^{-\kappa_2 z}, & \text{if } -d/2 < z < d/2 \\ De^{\kappa_3 z}, & \text{if } z < -d/2 \end{cases} \tag{3.10}$$

Then, by using 2.2, E_y is written as

$$E_y = H_{x0}e^{(j\beta y - j\omega t)} \begin{cases} -\frac{j\kappa_1}{\omega\epsilon_0\epsilon_1}Ae^{-\kappa_1 z}, & \text{if } z > d/2 \\ \frac{j\kappa_2}{\omega\epsilon_0\epsilon_2}Be^{\kappa_2 z} - \frac{j\kappa_2}{\omega\epsilon_0\epsilon_2}Ce^{-\kappa_2 z}, & \text{if } -d/2 < z < d/2 \\ \frac{j\kappa_3}{\omega\epsilon_0\epsilon_3}De^{\kappa_3 z}, & \text{if } z < -d/2 \end{cases} \tag{3.11}$$

where κ_n represents the wavenumber perpendicular to interface in Layer n. In the core region, no assumption is made relating the coefficients B and C. In fact, solutions of core region can be decomposed into two sets as even and odd solutions with respect to core center z=0. Here, we proceed with no assumption on symmetry, however, difference of both modes will be clear at the end of our derivation.

Then, by applying the requirement regarding continuity of tangential field components H_x and E_y; following relations can be written easily.

$$Ae^{-\kappa_1 \frac{d}{2}} = Be^{\kappa_2 \frac{d}{2}} + Ce^{-\kappa_2 \frac{d}{2}} \tag{3.12}$$

$$\frac{-\kappa_1}{\epsilon_1} Ae^{-\kappa_1 \frac{d}{2}} = \frac{\kappa_2}{\epsilon_2} Be^{\kappa_2 \frac{d}{2}} - \frac{\kappa_2}{\epsilon_2} Ce^{-\kappa_2 \frac{d}{2}} \tag{3.13}$$

$$De^{-\kappa_3 \frac{d}{2}} = Be^{-\kappa_2 \frac{d}{2}} + Ce^{\kappa_2 \frac{d}{2}} \tag{3.14}$$

$$\frac{\kappa_3}{\epsilon_3} De^{-\kappa_3 \frac{d}{2}} = \frac{\kappa_2}{\epsilon_2} Be^{-\kappa_2 \frac{d}{2}} - \frac{\kappa_2}{\epsilon_2} Ce^{-\kappa_2 \frac{d}{2}} \tag{3.15}$$

By solving 3.12-3.15 and $\beta^2 = k_0^2 \epsilon_n + \kappa_n^2$ for layer n=1,2,3; dispersion relation can be calculated numerically. For the case of symmetrical system where Layer 1 and Layer 3 are composed of same material, dispersion relation can be expressed in more simple way shown below.

$$\tanh(\kappa_2 d/2) = -\frac{\kappa_1 \epsilon_2}{\kappa_2 \epsilon_1} \tag{3.16}$$

$$\coth(\kappa_2 d/2) = -\frac{\kappa_1 \epsilon_2}{\kappa_2 \epsilon_1} \tag{3.17}$$

where κ_2 is the wavenumber in perpendicular to interface in Layer 2, and κ_1 is the wavenumber in Layer 1 and Layer 3 which are assumed to be identical. Two solutions shown by equation 3.16 and 3.17 indicate that there are two different mode distributions as even and odd symmetric for E_z, respectively. Relations 3.16 and 3.17 can be calculated numerically by employing a search algorithm for different material compositions and core thicknesses.

3.2 3D Plasmonic Waveguides

Two dimensional planar waveguides that employ surface plasmons have potential for confining modes to sub-wavelength volumes. Besides them, various three dimensional structures are proposed in the literature to have lateral confinement which is more suitable for dense packaging. Among them, mode characteristics and dispersion relation of the slot waveguides are well studied in the literature. [18]. There are also some studies that utilize such waveguides for designing optical components including modulators [41], multiplexers [42] and filters [43]. Hence, studies show that plasmonic waveguides with sub-wavelength gaps are promising for future optical chips thanks to their small fingerprints and moderate propagation lengths.

In this section, we will introduce three dimensional plasmonic waveguide geometries including slot waveguides and two wire transmission line waveguides (TWTLs). First, their dispersion relations and mode distributions will be introduced. Later, we will briefly investigate the effect of gap size, metal thickness and substrate material on the propagation characteristics.

3.2.1 Slot Waveguides

Slot waveguide geometry basically consists of a thick substrate and metallic pads which are separated by sub-wavelength gap as seen in Figure 3.5. The gap size and thickness of metallic pads are limited by fabrication-related issues which will be explained in the last chapter. The fundamental mode of this waveguide geometry is confined in the gap and dominant electric field component is polarized in y axis. The mode is propagating in $+x$ direction with $e^{(j\beta-\alpha)x}$ where β is the real part of the wavenumber and α is attenuation

constant. The relation between α and propagation length L_p is given as

$$L_p = 1/2\alpha \tag{3.18}$$

if L_p is defined as length at power of mode decays to its 1/e value.

Dispersion relation and mode distributions of three dimensional structures are unlikely to be solvable by analytical methods. Instead, we used finite-difference-time-domain solver package (Lumerical FDTD Solutions) to extract field distributions and dispersion relations for complex geometries. In FDTD method, a time pulse is used as excitation signal, then resulting fields are recorded in time-domain. To find the response of the system in each frequency point, Fourier transform is applied to time signals.

Fundamental mode of slot geometry is even symmetric for E_y fields, so, it reaches its maximum value at the center of waveguide. Thus, we placed a y-polarized single dipole at the center of waveguide in y - axis ($y = y_0$) and $x = x_0$ to excite the fundamental mode of the system. Simulation region is enclosed by perfectly-matched-layer (PML) boundary conditions. PML boundaries are assumed to be non-reflective, so it practically means that structure extends to infinity in the all directions.

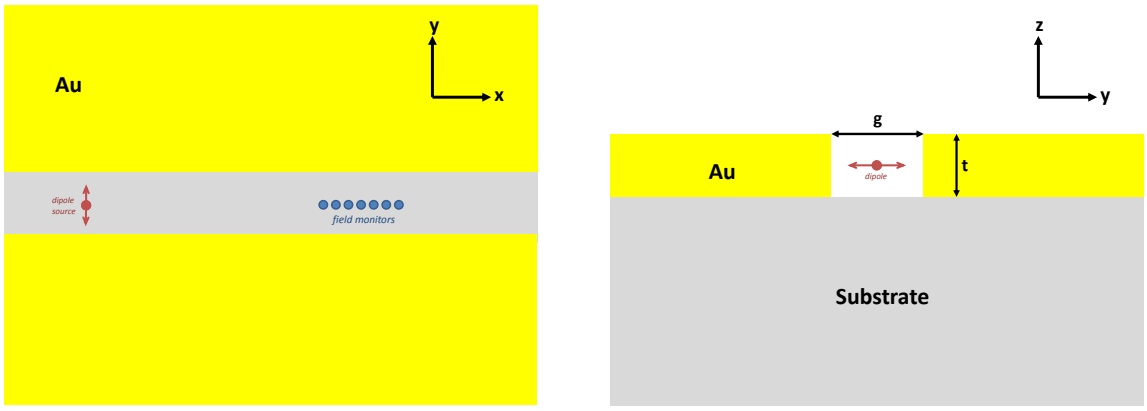

(a) Top view (b) Cross section view

Figure 3.4: Top and cross-section view of plasmonic slot waveguide, and placement of source and monitors for FDTD simulations.

Time-monitors that record dominant electric field component E_y are placed a few wavelengths away from the source to allow evanescent fields to decay away. Thus, we record the time variation (response to the dipole source) of electric field which belongs to fundamental mode by using equally spaced time monitors in x. The recorded fields are shown by $E_y(x_n, t_m)$ where x_n represents the spatial location of each monitor and t_m represents the points in time. Hence, $E_y(x_n, t_m)$ is represented by a $n \times m$ matrix composing of n spatial and m temporal points. The relation between time signal and its frequency components is given by taking temporal Fourier transform for each spatial location.

$$E_y(x_n, t_m) \xrightarrow{\mathscr{F}} E_y(x_n, \omega_m) \tag{3.19}$$

Resulting function composed of $n \times m$ matrix with n spatial points and m frequency points. Numerical values of each matrix element are given by the following relation where β_m and α_m are propagation and attenuation constants which belong to frequency ω_m, respectively.

$$E_y(n, m) = a_m e^{(j\beta_m - \alpha_m)x_n} \tag{3.20}$$

Then, for each frequency point m, n points array can be fitted to Equation 3.20 to find β_m and α_m. By using the the relation 3.18, L_p values for each frequency can be found easily.

This method enables us to find propagation characteristics of the mode for different frequencies by running a single simulation since we excite broad range of frequencies by pulse in time-domain. Frequency range is only limited by the limited-bandwidth source. In fact, if the there is a source at the desired frequency, the intended mode

is excited at that frequency. However, we are not distinguishing different modes since we are not solving the system for eigenmodes as in FDFD method. Instead, we record field propagation which is excited by dipole source to find propagation characteristics. Therefore, it is important to excite only the mode of interest. We are achieving this by placing a single dipole at the center of the waveguide for even modes, and placing π phase differenced two dipoles symmetrically located for odd modes.

Field distributions of the mode for different frequencies are also found by FDTD simulations. After exciting correct mode by the method explained above, a 2D monitor that records E and H fields is placed on the cross-section away from the excitation point. Taking temporal Fourier transform of each spatial point and mapping it will allow us to visualize field distributions in the specified frequency.

Dispersion Relations and Field Distributions

The dispersion relation and field distributions of simple slot waveguide geometry are found by using the method above. We used experimental permittivity data taken from Palik [25] for Au, and substrate is set as glass which has refractive index $n = 1.44$. Substrate thickness is set to ∞ by placing PML boundary conditions in the substrate direction. Gold thickness and gap size are set to 50 nm. By placing single dipole source at the center of y - axis, we guaranteed that the fundamental even mode is excited. Time monitors and field monitor are placed 3 μm away from the source not to be effected by evanescent fields which distort the fundamental mode. Figure 3.5 shows E field intensity and real part of E_y at the free space wavelength $\lambda = 1.55$ μm.

The mode of plasmonic slot waveguide is confined in the sub-wavelength gap whose dimensions are $\lambda/31$ in both directions. Figure 3.5b also reveals that dominant field component is even symmetric with respect to y-axis.

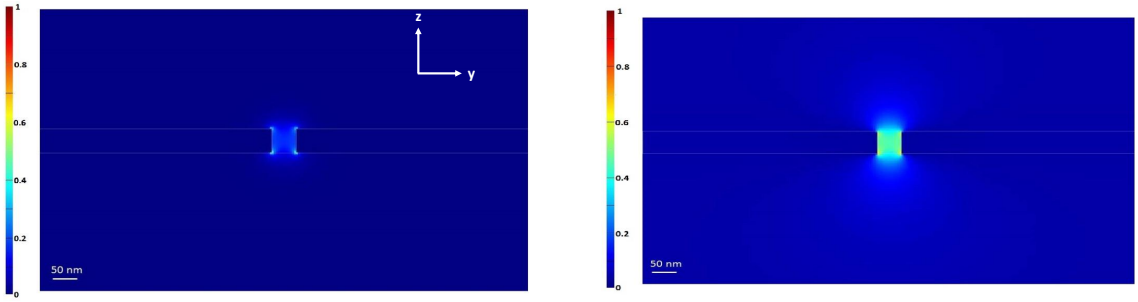

(a) Electric field intensity |E| (b) Real part of E_y

Figure 3.5: Electric field distribution of the fundamental mode of the slot waveguide at $\lambda = 1.55$ μm, where substrate is glass and 50 nm gold used as metal pads with 50 nm gap separation.

The Figure 3.6 shows dispersion relation of the fundamental mode with varying gap separation. As seen in Figure 3.6a, wavenumber is inversely proportional to gap size, i.e. as gap size increases real part of effective refractive index n_{eff} decreases. Figure 3.6b shows that waveguides with higher gap sizes have longer propagation lengths. This is explained as field confinement increases, propagation length decreases since more portion of the mode propagates in lossy metals [44].

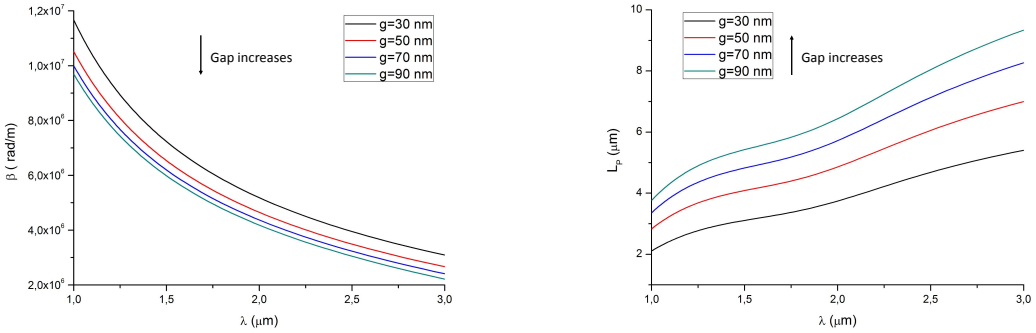

(a) Real part of the wavenumber (b) Propagation length

Figure 3.6: Dispersion relation of the fundamental slot mode with varying gap size.

The effect of thickness on propagation characteristics are examined in Figure 3.7. As seen in Figure 3.7a, β is inversely proportional to metal thickness which means thicker waveguides have lower n_{eff}. Figure 3.7b also shows that thicker waveguides have higher propagation length. However, thickness becomes less effective on mode characteristics

as it increases.

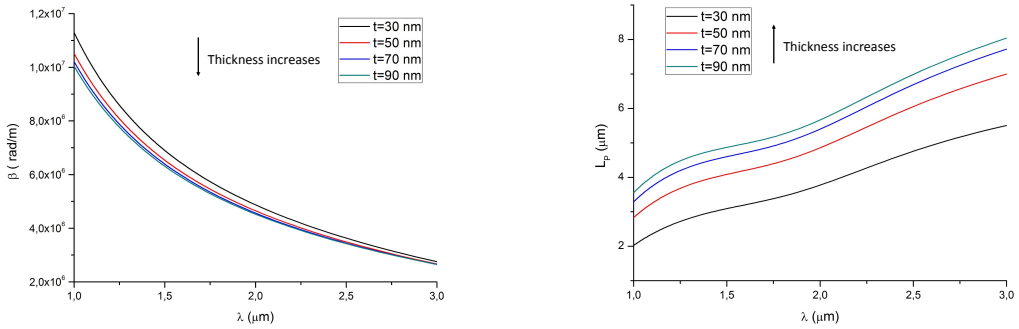

(a) Real part of the wavenumber (b) Propagation length

Figure 3.7: Dispersion relation of the fundamental slot mode with varying metal thickness.

Above analysis shows that fundamental mode of waveguide is well confined in the gap with even E_y field distribution. It is also revealed that propagation length is higher for higher metal thicknesses and higher gap sizes. Propagation length is around $4\mu m$ at $\lambda = 1.55\ \mu m$ for $t = 50\ nm$ and $g = 50\ nm$.

Substrate Effects

Fundamental mode of slot waveguide is always bound mode for the case of symmetric surrounding dielectric medium; it has no thickness, gap or wavelength dependent cutoff [18]. However, it is not the case for asymmetric geometries where the dielectric medium in below and above the metal films are different. Until now, the dispersion relation of slot waveguide with glass ($n_{glass} = 1.44$) substrate embedded in air ($n_{air} = 1$) is shown. However, we figured out that when we place silicon ($n_{silicon} = 3.4$) substrate instead of glass, there is no bound mode in the wavelength range of interest. This is caused by the high asymmetry between above and below medium, in fact bound modes always exist if metal films are surrounded by air, glass or silicon as far as surrounding medium is symmetric.

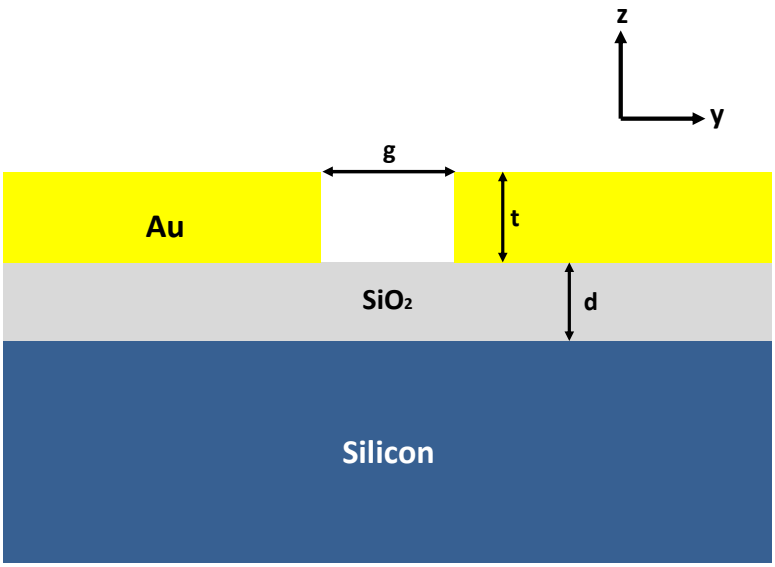

Figure 3.8: Cross section view of the plasmonic slot waveguide with modified substrate of $Si/Si0_2$.

On the other hand, silicon is very attractive material due to its manufacturability and its compatibility with mature CMOS technology that is used in VLSI circuits. Moreover, it has other advantages over glass substrate in terms of fabrication point of view where conducting substrates are easy to work with for electron beam lithography process. Due to these reasons, we aimed to keep silicon as a substrate material and to add an oxide layer between silicon substrate and metal films. Bounded modes are searched for such a geometry with varying oxide thicknesses. Figure 3.8 shows cross section view of slot waveguide which has $Si/Si0_2$ as substrate. Modes of this geometry are investigated for different thicknesses by using FEM (Comsol Multiphysics), and it is found that n_{eff}=1.578+0.0282i for d=500 nm and n_{eff}=1.580+0.0278i for the full glass substrate at $\lambda = 1.55$ μm, respectively. Hence, we conclude that 500 nm oxide layer is enough to have desired confined mode by keeping silicon as a substrate.

3.2.2 2-Wire Waveguides

Now we turn our attention to plasmonic two wire transmission line (TWTL) waveguides which have very similar geometry with slot waveguides. The only difference is finite metal width in y-axis. As a result of this, different than slot geometry, transmission line waveguides have both even and odd modes. The fundamental mode is even as in the infinite metal case and the fields are confined in the gap. On the contrary, for odd mode, fields are concentrated in outer edges of metal lines with odd symmetry of E_y.

Propagation characteristics of both modes are found with FDTD by using the same method as used for slot geometry. However, in this case, since we have both modes, we carefully excited desired mode by using different source placements. As seen in Figure 3.9a, for generating even modes, single dipole is placed at the center of the waveguide, whereas odd mode is excited by using two symmetrically located dipoles with π phase difference.(Figure 3.9b)

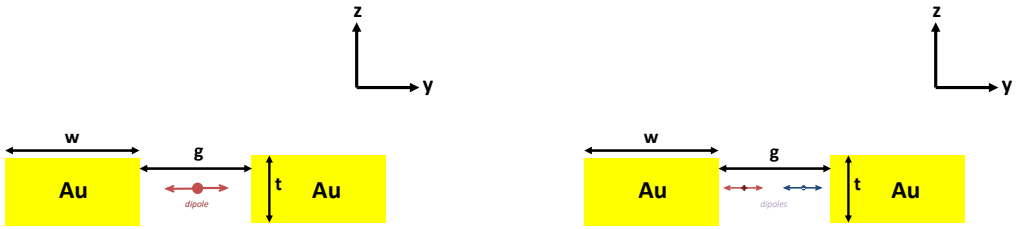

(a) y-polarized single dipole is placed at the center of the waveguide for the excitation of even modes

(b) y-polarized, π-phase differenced two dipoles are placed symmetrically for the excitation of odd modes

Figure 3.9: Cross section of 2-line plasmonic waveguide and excitation schemes for even and odd modes.

Field distributions are shown for the geometry of gap size 50 nm, metal width 75 nm and

thickness 50 nm. Metal lines are surrounded by air both as substrate and superstrate. Experimental data is used for gold permittivities which are taken from Palik [25]. As seen in Figure 3.10, fundamental even mode is very confined in the gap similar to slot waveguide. However, odd mode is mainly in the outer surface of metal lines.(Figure 3.11) Since metal width is infinite in the slot geometry, it is expected not to have this mode in the slot waveguide.

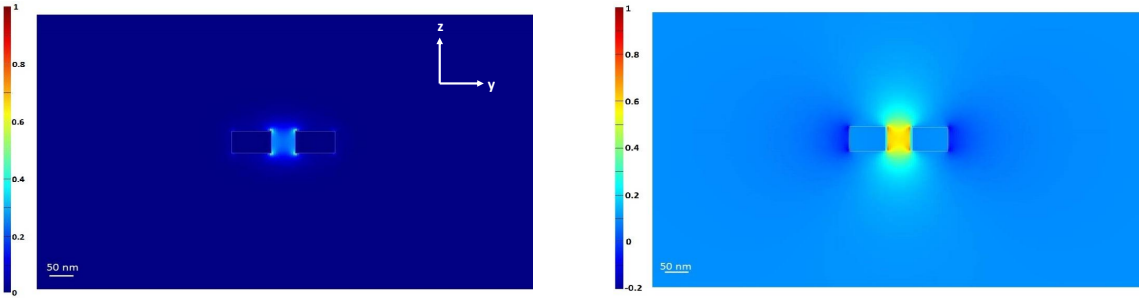

(a) Electric field intensity |E| (b) Real part of E_y

Figure 3.10: Electric field distribution of fundamental mode(even) of the plasmonic TWTL waveguide at $\lambda = 1.55\mu m$ for physical parameters of gap size 50 nm, gold width 75 nm and gold thickness 50 nm. Metal is surrounded by air.

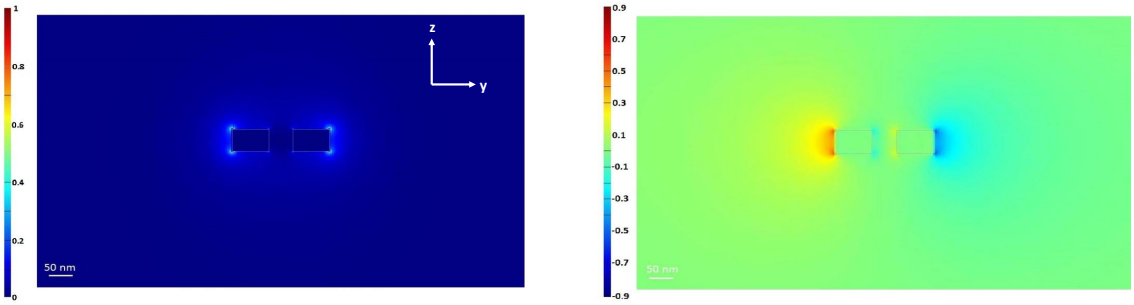

(a) Electric field intensity |E| (b) Real part of E_y

Figure 3.11: Electric field distribution of the odd mode of the plasmonic TWTL waveguide at $\lambda = 1.55\mu m$ for physical parameters of gap size 50 nm, gold width 75 nm and gold thickness 50 nm. Metal is surrounded by air.

Propagation characteristics of even mode with various gap sizes are shown in Figure 3.12. Metal thickness and width are kept constant as 50 nm and 75 nm, respectively. Similar to slot geometry, as gap increases propagation length increases and wavenumber

decreases. In this sense, even mode of the transmission line waveguide is very similar to fundamental mode of the slot waveguides.

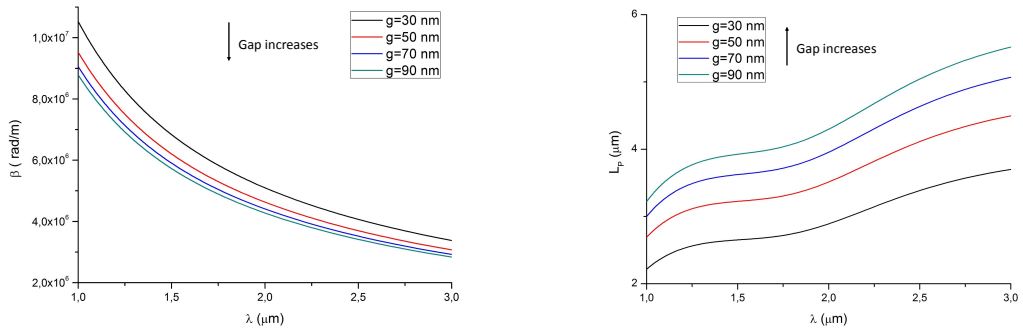

(a) Real part of the wavenumber (b) Propagation length

Figure 3.12: Dispersion relation of the fundamental mode of TWTL waveguide with varying gap separation. Metal width and thickness are kept constant as 75 nm and 50 nm, respectively. Gold pads are surrounded by air.

We also varied metal width to see the effect on dispersion. As seen in Figure 3.13, metal width greatly changes propagation length. For the w=25 nm, propagation length is below 2.5 μm in the frequency range of interest, and it goes to above 4 μm for w=150 nm. So, it can be concluded that as metal width increases, mode becomes less lossy, and the best case occurs for infinite metal width.

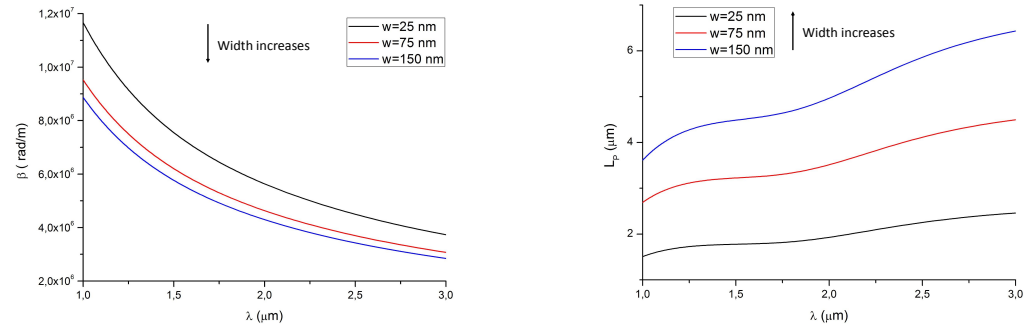

(a) Real part of the wavenumber (b) Propagation length

Figure 3.13: Dispersion relation of the fundamental mode of TWTL waveguide with varying metal width. Gap and and metal thickness are kept constant as 50 nm. Gold pads are surrounded by air.

After examining the effect of geometry parameters on the propagation characteristic, now we are at the point of summarizing differences. It is shown that asymmetric (odd)

modes have loose field distributions and they have longer propagation lengths. Therefore, they are more suitable for long range power delivery purposes. On the other hand, symmetrical modes have tight mode confinement with lower propagation lengths that makes them more suitable candidate for facilitating light-matter interactions. It is also concluded that, waveguides with smaller gaps have modes with lower effective wavelength with the cost of increased losses.

Chapter 4

Coupling to Waveguides

Plasmonic gap waveguides are examined in the previous chapter and it is concluded that they are promising for highly integrated optical interconnects thanks to their extreme sub-wavelength mode confinement and planar fabrication process. Utilizing such waveguides requires efficient excitation of the waveguide mode by an external light such as Gaussian beam. Also the propagating mode of the waveguide should be coupled to free space efficiently. However, until now not many studies have shown results for very efficient coupling to those waveguides from the free space.

The size of plasmonic gap mode of these waveguides are in the order of the gap dimensions, i.e. though there is no minimum theoretical limit, it is practically limited around 50 nm due to fabrication related issues, which creates high mode mismatch between free space Gaussian beams and the waveguide mode. In fact, this is the reason why the methods like end-fire coupling are not efficient for excitation of gap plasmons though it is a very well known method to couple light from optical fibers to the dielectric waveguides by matching spatial distributions [45]. There are also many studies showing coupling between dielectric and plasmonic waveguide by adiabatically decreasing the size of the mode to avoid reflections [46–48]. However, these methods do not offer solutions to the problem of free space to plasmon waveguide coupling.

A promising way is placing resonant scatterers, called plasmonic antennas, to the vicinity of waveguide ends. These scatterers, in most cases, scatter incoming light to multiple directions and some portion of it is coupled to waveguide. Efficiency of coupling can be

increased by controlling the shape and size of scatterers. In fact, there are studies that utilize plasmonic antennas like dipole antennas and bow-tie antennas for coupling to slot and transmission line geometries [49–51]. For schemes that use optical antennas, another way of enhancing coupling is placing reflectors around scatterers to have constructive interference, hence increased efficiency. Although some of the proposed solutions are not easy to fabricate with planar fabrication methods [52, 53], planar reflectors can also be configured to increase efficiencies [17, 54]. On the other hand, near field interactions between waveguides and antennas are also heavily dependent on impedance matching. In fact, there are numerous studies that show classical transmission line theories are applicable to plasmonic nano antennas [50, 55]. Therefore, one should consider many aspects to design efficient antenna couplers.

The other proposed solution in the literature is using grating couplers for the efficient excitation of plasmons. In fact, grating couplers are heavily used to couple to the two dimensional surface plasmon modes [56–58], but coupling to the highly confined waveguide modes are only the subject of few studies [59, 60]. Although they propose relatively higher efficiencies than single antennas, they are not compact in size, so they occupy great space on the chip which is not very compatible with small finger print devices.

By keeping explained constraints in mind, we aim to design efficient couplers between guided gap plasmons and free space photons. It is worth noting that fundamental mode of slot waveguides and plasmonic two-wire transmission lines are very similar to each other in terms of dispersion relation and mode distributions, so efficient interfaces between these two modes can be achieved easily. Therefore, designing of couplers whether using slot geometry or 2-wire transmission lines are not so critical in this stage since they can be transferred to each other.

In this chapter, we will start with demonstration of a plasmonic dipole antenna coupler

which couples light from Gaussian beam to the plasmonic slot waveguide or from waveguide mode to free space. The effect of geometrical parameters on the coupling efficiency and radiation characteristics will be investigated. Later, a few scatterer designs for two wire transmission line waveguides will be studied and their interaction with guided mode will be examined. In fact, they will be the building blocks of scatterer arrays which will be modeled in the next chapter.

4.1 Antenna Couplers for Slot Waveguide

In this section, a dipole antenna coupler that works at $\lambda = 1.55$ μm will be shown. Design steps and working principle of the antenna coupler will be examined by using finite-difference-time-domain (FDTD) simulations.

We begin with the description of the geometry. The gap size of plasmonic slot waveguide is set to 50 nm and gold is used as metal pads which has thickness 40 nm. Slot waveguide is positioned on a glass substrate which has refractive index $n = 1.44$. Geometrical parameters of waveguide kept same in the rest of the design. Coupler is placed at the opening of the waveguide as shown in the Figure 4.1.

Simulations are performed with commercial FDTD package (Lumerical Solutions). The mesh size is set as 5 nm in the vicinity of gap. In the rest of the simulation domain, non-uniform mesh is used. Simulation region is enclosed by perfectly matched layers (PML) that are not reflective to incoming fields. A Gaussian beam which has a beam waist of 1 μm is incident normally to the substrate and it is focused in the plane located 400 nm above the substrate surface. It is centered on the center of the antenna scatterer. Source electric field is polarized in y axis which is same polarization with antenna resonances and dominant electric field of waveguide mode. Then fields, so the transmitted power, are recorded 2 μm away from the waveguide opening on the cross

section of the waveguide. The size of power monitor is limited to 600 nm × 600 nm by centering it to the waveguide center, not to record power of any non guided modes. Since the slot geometry has only single guided mode, all the guided power in the gap belongs to the fundamental mode.

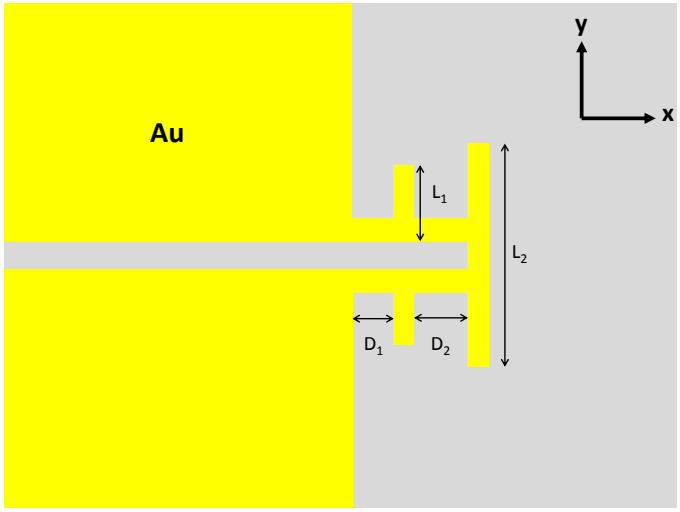

Figure 4.1: Top view of the slot waveguide and antennas placed at the opening of the waveguide. Fundamental mode of waveguide is confined in the gap with dominant electric field polarization in y-axis.

We employed particle swarm optimization algorithm to maximize light coupling at $\lambda = 1.55$ μm. Ratio of coupled guided power to the incoming total power is defined as coupling efficiency and it is determined as the figure of merit to optimize. First, L_1 and D_1 values are determined without putting back channel and reflector. We found that for this geometry best coupling occurs at $D1 = L1$ =200 nm, where both arms are behaving as coupled. Hence, total antenna length is consistent with single arm dipole antenna resonance which exists around 400 nm for the specified wavelength. Then, a non-resonant longer antenna is placed on the same xy plane, and it is used as back reflector that reflects scattered light in -x direction. Later, suitable values are searched for maximizing the figure of merit. In fact, this geometry is similar to previously studied designs [52, 54] with only minor differences. Previous studies used larger gap

waveguides, hence separation of arms are gradually decreased between waveguide and antenna. However, we used same gap opening with antenna arm separation. We also used a channel between back reflector and scatterer antenna to more efficiently reflect back scattered light to the waveguide. Coupling efficiency of our design is slightly lower than previous designs, but since we did not cover antennas with higher index material in the upper plane, lower values of coupling efficiencies are expected to see. The purpose of showing this geometry is to better see strong near field effects that make design steps complicated and to compare found coupling efficiencies with proposed designs which will be explained in the rest of thesis.

We found that for D_2 =200 nm and L_2 = 600 nm, a broadband coupling occurs around $\lambda = 1.55$ μm. Figure 4.2a compares coupling efficiencies of slot opening without antenna and with antenna. Around resonance frequency of the antenna, coupling is enhanced by at least 10 times compared to bare opening and it reaches values close to 5 %. The field distribution (absolute value of E_y) at the plane 20 nm above the substrate is also shown in Figure 4.2b. It is clear that at the resonance wavelength, first antenna is excited and longer back antenna acts as reflector.

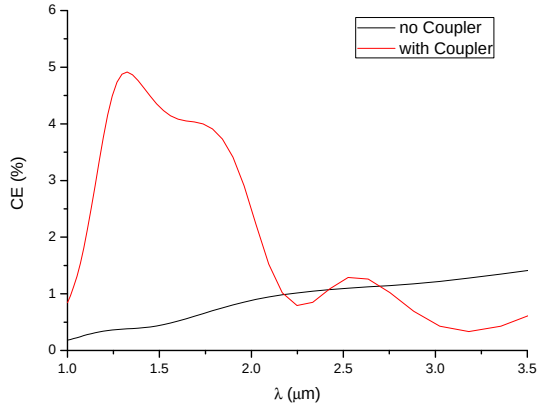

(a) Coupling efficiency

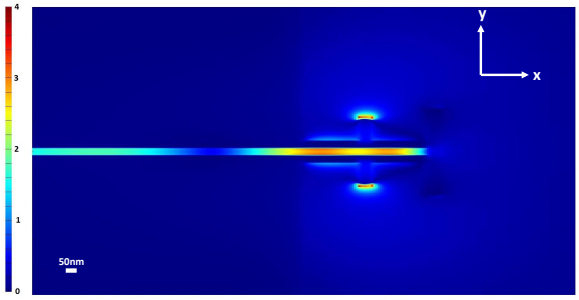

(b) Absolute E_y distribution at the resonance wavelength

Figure 4.2: Coupling efficiency and field distributions for the designed antenna which is placed at the opening of the slot waveguide.

Coupling enhancement shows that resonant antennas act as scatterers that interact with

incoming Gaussian beam, but coupling efficiency is limited due to a few reasons [52]. To name, some of the power is lost due to increased losses at the resonance wavelength. The other reason is such excited antennas radiate in multiple directions, in fact, more efficiently to the direction of higher index materials. In our case, glass has refractive index higher than air, hence total radiated power to the substrate is higher than total radiated power to the air. The other way of saying is, antennas are easier to excite when the beam is sent from the higher index material. Therefore, coupling efficiency is limited when the beam is sent from the air instead of higher index substrate. Moreover, due to impedance matching, not all of the power scattered in the waveguide direction is able to be launched in the waveguide. Also due to complicated scattering process of such sub-wavelength structures, various other effects may exist which are hard to model.

4.2 Strengths of Integrated Scatterers

The behavior of such antenna couplers placed at the openings of waveguides are not easy to understand since near field interactions in the vicinity of slot opening make the scattering process very complicated. Hence, analytical modeling of such a system is hard to deal with, in fact we heavily used optimization methods to find previous design geometry. Instead of locating these scatterers at the end of a waveguide, one other way is to embed antenna couplers within a waveguide so as to eliminate additional scattering effects caused by the waveguide openings. Here, we will investigate resonance properties of such scatterers and then their potential applications as couplers will be discussed. Using embedded antennas with slot geometry shown before is not possible, instead two-line transmission line waveguides (TWTL) will be used.

In this section we will investigate scattering strengths of embedded antennas by sending waveguide mode as input (as in Section 3.2) and recording the out coupled light to

the upper xy plane. Air is chosen as symmetrical surrounding medium to interpret results easier. Gold is chosen as metal with experimental permittivity values taken from literature [25]. We fixed metal width (w) as 75 nm and metal thickness (t) as 50 nm. Simulation region is surrounded by PML not to have any reflecting fields from boundaries. Mesh size is set to 5 nm in the vicinity of waveguide lines and the gap.

4.2.1 Even and Odd Mode Excitation

The fundamental mode of finite and infinite metal width plasmonic slot waveguides resembles to each other, transition from one type waveguide to other one can be achieved easily by using adiabatic change in metal width. However, it is worth noting that TWTLs have both even and odd symmetric guided modes, so antenna and guided mode interactions will be studied for each case separately. We, first, started with comparing the behavior of dipole antenna pair (shown in Figure 4.3) for even and odd mode excitations.

Figure 4.3 shows the top view of the TWTL waveguides with integrated dipole antenna pair. The resonating single metal rods are defined as dipole antennas in the literature [61] and we follow this definition when we talk about dipole antennas. The length of symmetrical antenna pair is determined by the resonance condition at $\lambda = 1.55$ μm. Even and odd modes are generated at the source plane (yz plane) as separate cases, and transmitted and reflected fields are recorded at T and R planes. Intentionally, cross sectional size of these monitors are chosen comparable to the mode size not to record free propagating waves that are created by scattering. Also, a power monitor is placed 400 nm above the waveguide to record scattered fields in the upward direction. Since the system is symmetric in z axis, total scattered power in the upper and the lower regions are equal to each other.

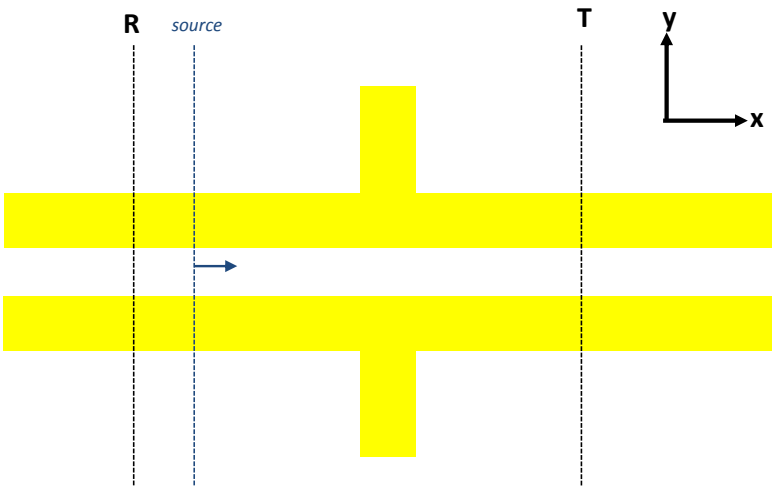

Figure 4.3: Top view of the antenna embedded TWTL waveguide geometry. Source, reflection and transmission planes are shown by dotted lines.

This geometry is first studied for excitation with fundamental (even E_y) modes. Span of antenna in x direction and waveguide gap are set to 50 nm, and by playing with the arm length(l) of the each symmetrical antenna pairs, resonance at $\lambda = 1.55$ μm is achieved for $l = 220$ nm. Resonance is determined as the wavelength where antenna scatters most power in the upward and downward planes. Hence, it is assumed that a peak in scattering curve shows the resonance wavelength. Interestingly, found l value is much less than expected, in fact for a single arm dipole surrounded by air resonates at 1.55 μm for l =500 nm. That shows that each arm is not behaving independently with respect to each other. We first suspected from coupling between antenna arms, though 50 nm gap separation is a high distance for such a coupling to occur between antenna arms. To confirm our predictions, the effect of waveguide gap size on the resonance wavelength is investigated. We also simulated the asymmetrical one-arm antenna whether to see any shift in the resonance. Figure 4.4 shows scattering results for two symmetrical antennas with l =220 nm attached to waveguides with gap size of 50 nm, 80 nm and 100 nm and single antenna attached to waveguide of 50 nm gap. Scattering is recorded only

in the upper plane, due to the symmetry, total scattering is in upward and downward directions are double of percentage scattering values shown in Figure 4.4.

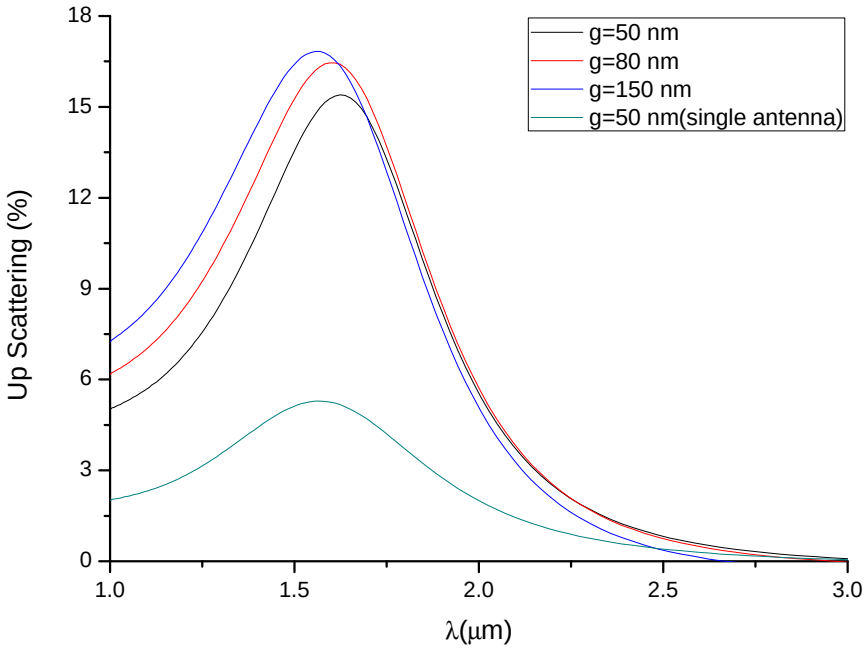

Figure 4.4: Scattered power ratios to the upper plane for different gap separations, when the fundamental (even) mode is excited in the.

As seen in scattering curve, antennas scatter more efficiently for the case of higher gap sizes. For instance for the gap size of 150 nm, two antennas scatter around 33 % of the incoming guided mode into upward and downward directions. It is also worth noting that when gap size decreases by keeping antenna arm lengths as fixed, resonance shifts to higher wavelengths, i.e. black curve that belongs to g=50 nm shows a resonance peak at $\lambda = 1.68$ μm and at the same time resonance peak slightly decreases. Therefore, we conclude that when such a system is excited by fundamental mode of the waveguide, antennas efficiently scatter light by possessing resonances which is not same with known dipole resonances.

We performed similar analysis for the odd-symmetric mode of the TWTL waveguide geometry. The only difference, waveguide is excited for odd mode instead of fundamental mode of the system. Figure 4.5 shows scattering powers for various antenna arrange-

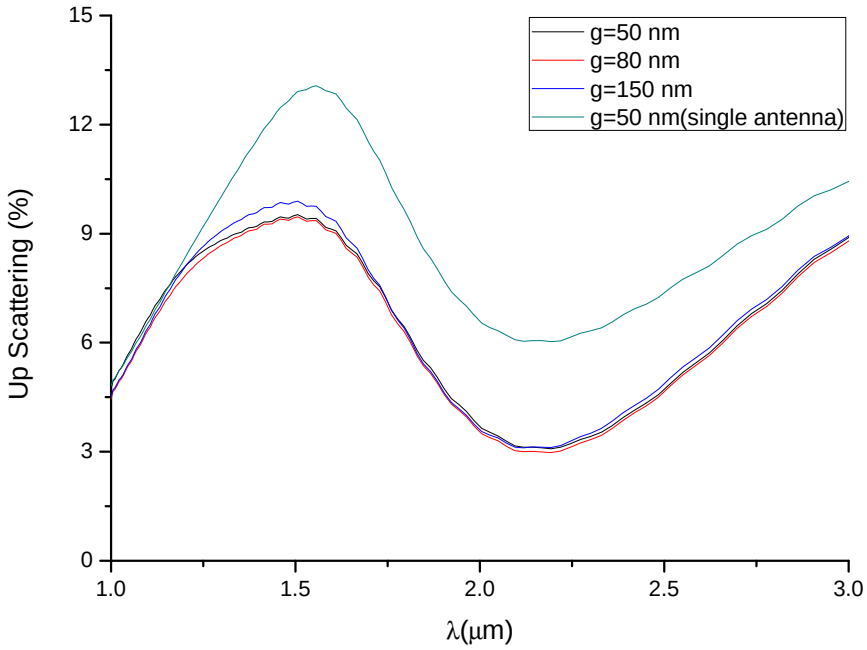

Figure 4.5: Scattered power ratios to the upper plane for different gap separations, when the odd mode is excited in the waveguide.

ments as in the previous case. Scattering curve shows that, single antenna performs better than two antennas, and red shift seen in the previous case does not exist. Hence, for this scheme, having two antennas does not enhance the scattering instead they have diminishing effect on the total scattered power.

The difference between two mode behavior can be understood by comparing field distributions in the both cases. Figure 4.6 shows real part of E_y at the resonance of double antennas for even and odd symmetric modes. Recorded field plane is located at the xy cross section of z =25 nm. When the antennas are excited with even symmetric fundamental mode, both arms are resonating in phase and they constructively support the radiated power. However, for the odd mode, major driving field of E_y at the each antenna arm are in opposite phase with respect to each other, hence they have less total radiation compared to single antenna case. We conclude, by looking at this difference, that even waveguide modes are more appropriate to drive radiative modes of the antenna.

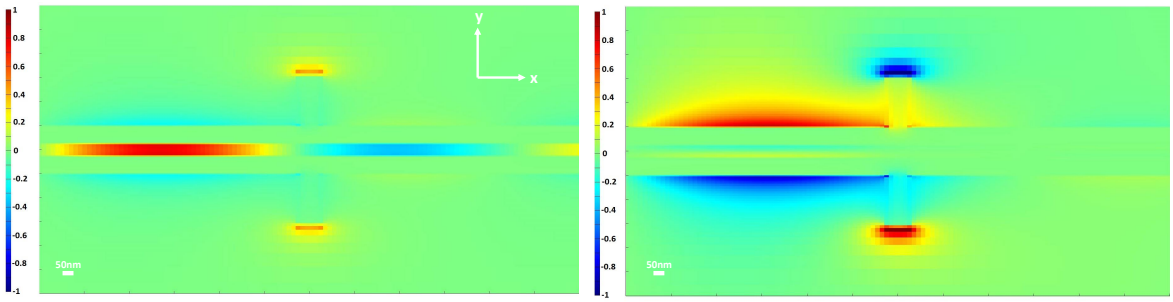

(a) Even mode is excited (b) Odd mode is excited

Figure 4.6: Real part of E_y at the resonance wavelength of each antenna.

To summarize, fundamental mode of the waveguide is scattered and out coupled to free space by employing resonant antennas. The scattering intensity and reflected power are enhanced by placing two arms of resonant antennas. Hence, two arm antenna is more preferred for coupling purposes.

4.2.2 Differences of Integrated Scatterers

In this section, we compared three scatterer configurations (one is the same design in Section 4.2.1) to see their behavioral differences on transmission, reflection and scattering. We did this since those designs will be building blocks of more complex scatterers which will be explained in the next chapter. The structure in Figure 4.7b shows a single arm longer antenna with no gap separation which is resonant at $\lambda = 1.55$ μm. This geometry, in fact, is like simple dipole antenna that exists in the literature. The next one (Figure 4.7c), is a simple obstacle which closes the opening of waveguide.

Same analysis as in Section 4.2.1 is performed for scattering efficiency calculations of new designs. Also, transmission and reflection efficiencies are calculated for all designs. The transmitted and reflected powers are recorded in the planes shown in Figure 4.3, but then they are effectively carried to antenna location by compensating the losses due to propagation between antenna and monitor location. Hence attenuation effects due

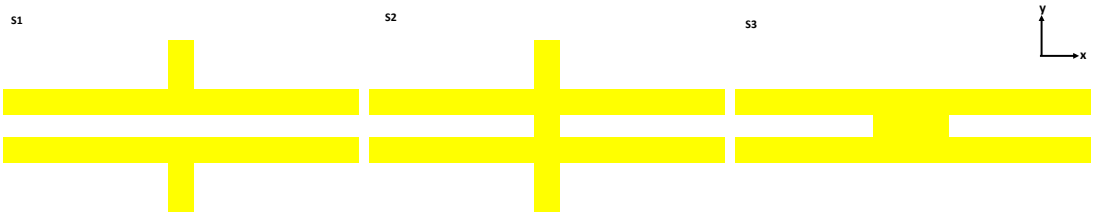

(a) Design S1: 2 Antenna Arm Pairs (b) Design S2: Single Arm Antenna (c) Design S3: Closed Waveguide

Figure 4.7: Different scatterer geometries embedded in TWTL waveguide.

to propagation are discarded. Although, recorded powers in transmission and reflection planes are not necessarily only the guided powers, we confirmed that they essentially belong to guided mode by performing mode expansion in those planes.

The Figure 4.8 compares three configurations with respect to their coupling, reflection and transmission properties. The first conclusion is that design S2 scatters more efficient than S1 by reaching 15% in upward direction. Design S3 has almost no transmission and very low scattering. However, it has very high (more than 90 %) reflection in the frequency range of interest.

The other obvious difference is reflection of S2 has a dip in the resonance whereas S1 peaks its reflection at the resonance wavelength. For the transmission, behavior of two are opposite and S1 shows a dip at resonance. This difference is explained as follows: S1 simply works as disturbance to the waveguide mode around the resonance wavelength, it simply reflects light at the resonance by allowing it to pass in other wavelengths. On the other hand, S2 acts as a barrier to the waveguide mode (as for S3), hence out of resonance it only transmits small portion of incoming mode. However, at the resonance, due to its scattering in multiple direction, scattered light couples back effectively to propagating mode as a transmission. This effect is more clear for the case of S3, since it has no resonance in the range of interest, it simply blocks the waveguide mode with

very less scattering in upward and almost zero transmission to waveguide mode. Hence, the both S2 and S3 are blockade to waveguide mode with a difference that S2 has a resonance in the simulated wavelength range.

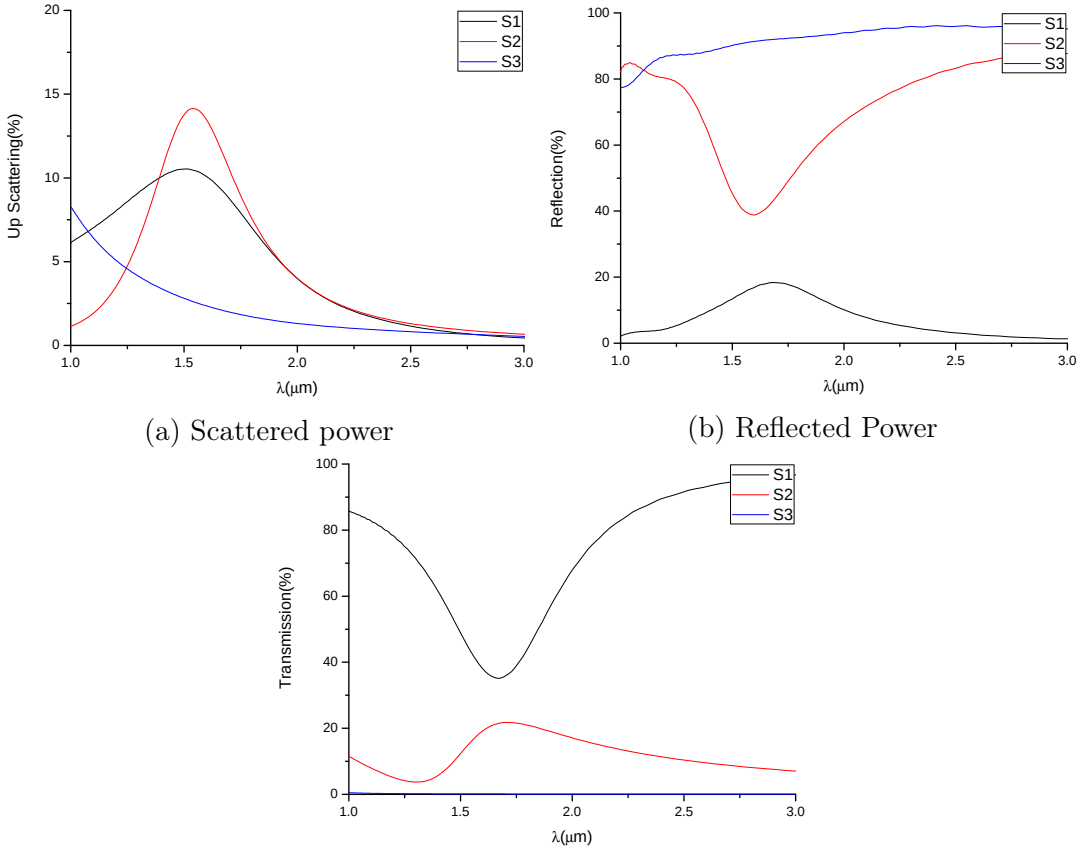

(a) Scattered power

(b) Reflected Power

(c) Transmitted Power

Figure 4.8: Comparison of scattering, reflection and transmission for geometries S1,S2, and S3.

To conclude, each geometries S1,S2 and S3 have different advantages over others in terms of their coupling, transmission and reflection characteristics. In fact, this is an exciting result, since they can be arranged as an array to couple light more efficiently to the free space by decreasing reflection and transmission values. By utilizing them, one can come up with smart designs such as efficient couplers. For instance, such building blocks can be used as components of scatterer arrays. In fact, we will be examining such more complex designs in the next chapter.

Chapter 5

Modeling of Integrated Antennas as Efficient Couplers and Angle Dependent Radiators

Plasmonic antenna couplers which are placed at openings of slot waveguides are shown in the previous chapter. Although those designs can be optimized to couple the incoming Gaussian beam to the waveguide mode or to couple injected waveguide mode to the free space, optimization is fully computational procedure that lacks a model for the nature of coupling. In fact, due to strong near field interactions around the waveguide opening and antennas, controlling coupling efficiency and angle of radiation is not possible. One proposed way of decreasing complex near field effects and having more control over coupling and radiation characteristics is embedding these scatterers in the waveguide instead of locating them around slot ends. We have shown that antennas embedded in transmission line waveguides can be used to scatter light and eventually to couple it to the free space. We followed only computational methods to find appropriate design parameters in the previous chapter. We also did not mention their angle dependent radiation characteristics. In this chapter, we will propose ways of manipulating their coupling efficiencies and angle of radiation, by using a semi-analytical approach.

Modeling of antennas will not only give us more solid understanding but also the cost of optimization will be decreased since the behavior of them will be more predictable. In fact, using optimization methods for designing nanophotonic components are very common in the literature. However, FDTD simulations are time-consuming and require

high computational powers which are not appropriate for blind try and see methods. Hence, design of such photonic structures by only using optimization requires a lot computational effort. Instead, more analytical approaches are required to engineer them. In fact, recent studies that employ semi-analytical approaches to design photonic components have taken attention due to their clear advantages on design formalism [62]. In the current literature, there are only studies that model antennas and waveguides with impedance concepts, however they are not providing information about the angle of out-coupled radiation. On the other hand, there is no literature on the control of angle-dependent radiation for geometries which employ plasmonic waveguide and plasmonic antennas. Controlling angle of radiation is, on the other hand, very crucial to increase the coupling since objective lenses and fibers have finite numerical aperture, hence they can only collect the light in the cone with a finite angle. Therefore, the direction of out-coupled light and its angular distribution are crucial to understand and to control for better designs. We show that this problem can be managed by using embedded antennas as an array of radiators and modeling their excitation amplitudes with S-matrix formalism.

In this chapter, first we will give review of necessary mathematical tools which are employed for developing our modeling approach. Later, we will introduce S-matrix method to model array of integrated scatterers. These scatterers are basically plasmonic antennas separated by variable distances along the propagation axis. Then, modeling results for transmission, reflection and coupling will be demonstrated for arrayed antennas and they will be compared with FDTD results. Finally, a sample design for coupling from the waveguide to the free space and from the Gaussian beam to the waveguide mode will be shown.

5.1 Theoretical Background

5.1.1 S-Matrix

A 2-port photonic system can be modeled by 4-element matrix that relates the incoming fields to the outgoing fields. This system matrix is called *scattering matrix* (S-matrix). The closed box in Figure 5.1 represents any linear system without loss of generality where a_1 and a_2 are amplitudes of fields entering to the box and b_1 and b_2 are amplitudes of fields leaving the box. When there are multiple scatterers periodically or aperiodically located next to each other, S-matrix approach can be used to find overall response of the system. For instance, it is very commonly used method to model the behavior of Bragg reflectors which are composed of periodic array of different materials that behave as good reflector in the designed wavelength. Although, S-matrix method is widely used in slab geometries where plane waves impinge on them, same approach can also be applied to waveguide ports where a and b coefficients represent amplitudes of the related waveguide mode.

For such a linear system, the relation between elements of S-matrix and input/output variables are shown below. In our system, a and b will be representing amplitudes of propagating waveguide mode.

$$b_1 = S_{11}a_1 + S_{12}a_2 \tag{5.1a}$$

$$b_2 = S_{21}a_1 + S_{22}a_2 \tag{5.1b}$$

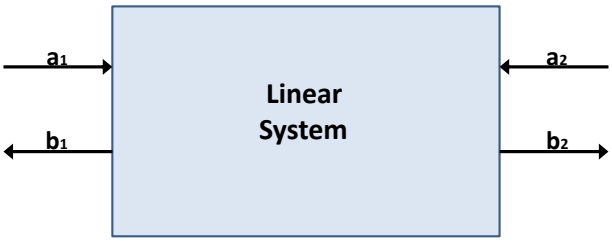

Figure 5.1: A linear system represented by closed box can be modeled by S-matrix by defining input and output ports as a and b, respectively.

These two equations can be written in the matrix form as follows,

$$\mathbf{b} = \mathbf{S}\mathbf{a} \tag{5.2}$$

where **a** and **b** are column vectors that represent incoming and outgoing field amplitudes, respectively.

$$\mathbf{a} = \begin{bmatrix} a_1 \\ a_2 \end{bmatrix} \qquad \mathbf{b} = \begin{bmatrix} b_1 \\ b_2 \end{bmatrix}$$

By this definition, S-matrix of two-port system is composed of four complex elements as shown below.

$$\mathbf{S} = \begin{bmatrix} S_{11} & S_{12} \\ S_{21} & S_{22} \end{bmatrix}$$

For a specific class of medium, one can define special constraints on the properties of scattering matrix elements. If the closed box is a reciprocal media where permittivity

and permeability are direction independent, one can show that $S_{12} = S_{21}$. Moreover, for lossless systems, scattering matrix becomes unitary, and the following conditions should be satisfied [63].

$$|S_{11}|^2 + |S_{12}|^2 = 1 \tag{5.3a}$$

$$|S_{21}|^2 + |S_{22}|^2 = 1 \tag{5.3b}$$

$$S_{11}^* S_{12} + S_{21}^* S_{22} = 0 \tag{5.3c}$$

For the cascade connection of scatterers, overall scattering matrix is not simply product of individual scattering matrices. For such a connection, one should calculate *transfer matrix* $\mathbf{T}$ of the each scatterer which basically defines the relation between the field amplitudes of each port namely, port 1 and port 2 in the our system.

$$\begin{bmatrix} b_2 \\ a_2 \end{bmatrix} = \begin{bmatrix} T_{11} & T_{12} \\ T_{21} & T_{22} \end{bmatrix} \begin{bmatrix} a_1 \\ b_1 \end{bmatrix}$$

Although both scattering and transfer matrices carry the scattering information, these two quantities are not same and one should perform a transformation to get the other from the one. Fortunately, this transformation can be managed easily as follows

$$T_{11} = S_{21} - \frac{S_{11}S_{22}}{S_{12}} \qquad T_{12} = \frac{S_{22}}{S_{12}}$$

$$T_{21} = -\frac{S_{11}}{S_{12}} \qquad T_{22} = \frac{1}{S_{12}}$$

After calculating transfer matrix representation of each scatterer one can express overall transfer matrix of such system $\mathbf{T_t}$ as the product of transfer matrix of each scatterer.

For a sample system of three different elements, overall transfer matrix is shown below.

$$\mathbf{T}_t = \mathbf{T}_1\mathbf{T}_2\mathbf{T}_3 \tag{5.4}$$

Transfer and scattering matrix approaches give us opportunity to calculate overall transmission and reflection of the cascaded system by simple matrix multiplication. Moreover, by this method, we can calculate the field amplitudes before and after than each scatterer. Field amplitudes that excite each scatterer will be later used to calculate overall scattering in upward and downward directions. Since antenna scatterers of such a system is placed next to each other with sub-wavelength separation, overall system will act as an antenna array, hence for the calculation of angle dependent total scattered power, antenna array approach will be employed.

5.1.2 Antenna Arrays

Antennas are simply radiating or receiving elements that convert electric signal (or guided waves in a transmission line) to the propagating electromagnetic waves or vice versa. In this respect, we can treat our waveguide-integrated scatterers as antennas, since they can convert confined guided mode into propagating free space radiation. In some RF applications, antennas are specially designed with directive properties to capture incoming light in the one specific direction. In fact, same approach can be employed in our system of scatterers.

Radiative elements that are fed by transmission lines can be arranged in the space for directional radiation. Such configured multiple antenna elements are called *antenna arrays* and they offer unique properties such as beam steering and gain enhancement. Radiation pattern of antenna arrays are both dependent on geometrical placement of

antennas and relative amplitude and phase of each antenna feeder. The latter is called *phased array* and they have wide application range particularly for radars. Here we will give a brief background on the calculation of radiation pattern of antennas by taking into account their excitation amplitudes and geometrical arrangement.

An antenna array composed of two identical scatterers are shown in Figure 5.2. Here each antenna element is shown by dots where s_1 and s_2 represent their excitation amplitude. This is the case in practice since excitation of each element does not have to be same and it can be controlled by playing with arrangements of scatterers. Scatterers are separated by L_1 and L_2 from the origin where θ is defined from the $+x$ direction. These scatterers are located in the same y coordinate, hence system is symmetric with respect to y - axis. Although this formalism can be generalized for n number of array elements we will stick to two elements during derivations for simplicity.

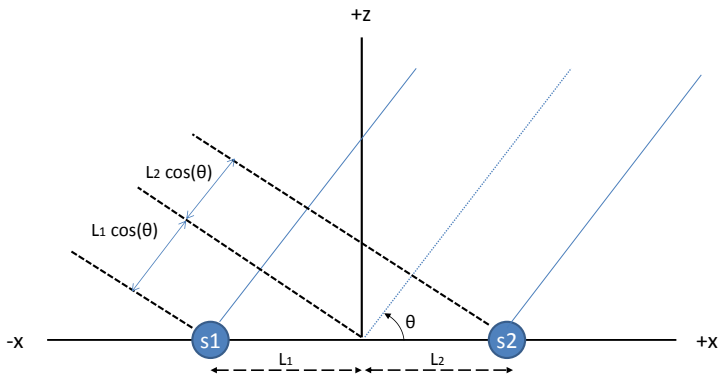

Figure 5.2: Geometrical representation of two element scatterer array. Rays are used to for radiation pattern calculation.

Radiation pattern of such antenna array is determined by radiation pattern of each antenna element (element factor) and their placement with respect to each other. For mathematical derivation of array effect, antenna elements will be regarded as isotropic

sources that radiate equally in every direction (hence their element factor will be taken as constant), and resulting radiation pattern of the array will be called *array factor*. This approach is very useful since for array of identical antennas, overall radiation pattern is given by multiplication of radiation pattern of each element (element factor) and array factor. Hence, if one knows the array factor of the configuration, overall radiation pattern R can be calculated by multiplying angle dependent element factor and array factor.

$$R(\theta, \phi) = E(\theta, \phi) AF(\theta, \phi) \tag{5.5}$$

For such a system overall radiated power is also angle dependent. If we normalize total radiated power with respect to radiated power of each element, total power enhancement can be found as follows.

$$P_{enhancement} = \frac{\int_{\theta,\phi} |R(\theta,\phi)|^2 \mathrm{d}\theta \mathrm{d}\phi}{\int_{\theta,\phi} |E(\theta,\phi)|^2 \mathrm{d}\theta \mathrm{d}\phi} = \frac{\int_{\theta,\phi} |E(\theta,\phi)|^2 |AF(\theta,\phi)|^2 \mathrm{d}\theta \mathrm{d}\phi}{\int_{\theta,\phi} |E(\theta,\phi)|^2 \mathrm{d}\theta \mathrm{d}\phi} \tag{5.6}$$

Now, we turn our attention to the calculation of array factor. As explained above, array factor is only dependent on the placement of sources and their relative excitation with respect to each other. For a single isotropic radiator located at the origin, radiated fields are proportional to $\propto s\frac{e^{+j\beta r}}{4\pi r}$ where s is the complex excitation amplitude of radiator, β is the wavenumber in the frequency of interest and r is the distance between observation point and origin. Hence, for a single radiator, radiation is angle-independent and array factor is represented by a scalar number $AF = s$. However, when two radiators are placed as in the Figure 5.2, radiated waves from each scatterers will experience different path for a fixed angle before reaching the point of observation. Therefore, fields at the observation point will be dependent on excitation amplitude, relative phase of each source and their distance to the observation point. For the above figure, overall radiation

can be written as follows by considering phase accumulation effects.

$$R = (s_1 \times \frac{e^{+j\beta r_1}}{4\pi r_1}) + (s_2 \times \frac{e^{+j\beta r_2}}{4\pi r_2}) \tag{5.7}$$

where r_1 and r_2 are distances between observation points and scatterers. At the far field where $r \gg L_1$ and $r \gg L_2$, equation 5.7 can be approximated as follows.

$$R = (s_1 \times \frac{e^{+j\beta(r+L_1 cos(\theta))}}{4\pi r}) + (s_2 \times \frac{e^{+j\beta(r-L_2 cos(\theta))}}{4\pi r}) \tag{5.8}$$

Then, array factor of two element is written as

$$AF(\theta) = s_1 e^{+j\beta L_1 cos(\theta)} + s_2 e^{-j\beta L_2 cos(\theta)} \tag{5.9}$$

Here we showed array factor of two element displaced only in x-axis for simplicity. Actually, same procedure can be applied to any number of antenna elements which are arbitrarily located. In general, AF is both θ and ϕ dependent variable.

5.2 Modeling with S-Matrix

Dipole antennas embedded in transmission line waveguides which are excited by the waveguide mode radiate in all directions, which is a complex scattering process itself. We already shown that they can reflect the incoming light to the waveguide mode back or transmit some of the power forth to the waveguide mode again. The rest of the power is radiated to free space or lost due to material losses during scattering process. Hence, the light coupled to free space constitutes a little portion of all power since the majority of power is reflected and transmitted with ratios varying with wavelength.

Although material losses are inevitable during the scattering process, we propose that by using array of scattering antennas one can reduce the reflection or the transmission by adjusting the phases of scatterers constructively or destructively. Also placing more than one scatterer will enable us to increase the out-coupled light since it will allow us to excite more antennas. However, since those scatterers are placed very close to each other along the propagation axis, total radiated power will not be simply the sum of excitation amplitudes instead one should consider the array effect. Due to the array effect, radiated power will be angle dependent. To summarize, arrayed antennas give us opportunity not only to decrease reflected and transmitted light but also to play with the angle of out coupled light.

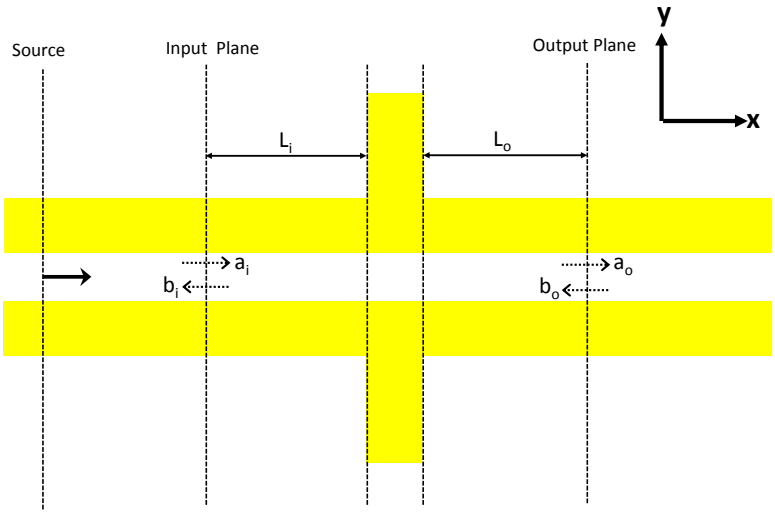

Figure 5.3: Simulation scheme that is used to find S-parameters of single scatterer element.

We begin modeling of our system by finding S-matrix parameters of dipole antenna scatterers. Figure 5.3 shows top view of the simulation setup for finding S-parameters of antenna scatterer. Fundamental mode of the transmission line waveguide is excited at the source plane. This mode is propagating in $+x$ direction, and it is scattered by the antenna located at the origin. Input and output planes are placed at a distance

of L_i and L_o from the scatterer, respectively. Then, fields at the cross section of input and output planes are recorded by field monitors. Those planes are intentionally placed away from the scatterer not to be affected from evanescent fields that scattering might cause.

If one knows the complete set of basis modes of a waveguide, any combination of guided modes in a plane can be expressed as

$$\mathbf{E}_{in} = \sum_m a_m \mathbf{E}_m^{forward} + b_m \mathbf{E}_m^{backward} \tag{5.10}$$

$$\mathbf{H}_{in} = \sum_m a_m \mathbf{H}_m^{forward} + b_m \mathbf{H}_m^{backward} \tag{5.11}$$

where each m represents a mode in basis, $\mathbf{E}_{in}$ and $\mathbf{H}_{in}$ are fields recorded in the plane of expansion, a_m and b_m are amplitudes of guided mode m in forward and backward directions, respectively. Here $\mathbf{E}_m^{forward}$ and $\mathbf{E}_m^{backward}$ have same field distribution with opposite phase factors. The amplitude coefficients can be given by taking spatial overlap integral on the mode cross section by using the following relations [64].

$$a_m = 0.25 \times \left(\frac{\int d\mathbf{S} \cdot \mathbf{E}_{in} \times \mathbf{H}_m^*}{N_m} + \frac{\int d\mathbf{S} \cdot \mathbf{E}_m^* \times \mathbf{H}_{in}}{N_m} \right) \tag{5.12}$$

$$b_m = 0.25 \times \left(\frac{\int d\mathbf{S} \cdot \mathbf{E}_{in} \times \mathbf{H}_m^*}{N_m} - \frac{\int d\mathbf{S} \cdot \mathbf{E}_m^* \times \mathbf{H}_{in}}{N_m} \right) \tag{5.13}$$

$$N_m = 0.5 \times \int d\mathbf{S} \cdot \mathbf{E}_m \times \mathbf{H}_m^* \tag{5.14}$$

Equations 5.12-5.14 are valid for lossless waveguides. For lossy waveguides, although orthogonality relation is expressed without conjugate signs [65] we used above expressions since Lumerical FDTD package comes with compact way of calculating them. For our simulations, we first assumed that scattered power is only coupled to fundamental mode of the waveguide. Hence, the fields at the input and the output planes are expanded

for the fundamental mode of the system by using the Equations 5.10-5.14 to find their relative amplitudes. We have used the fundamental mode distributions calculated by Lumerical and recorded field data in the input and output planes for mode expansions. Hence, a and b coefficients are found at the input and output planes. Here a_i and b_i represent mode amplitudes of fundamental mode at the input plane propagating forward and backward directions, respectively. Similarly, a_o and b_o represent mode amplitudes of fundamental mode at the output plane propagating forward and backward directions, respectively.

Next, S-parameters of single antenna are calculated. We assumed that system is composed of two ports only, i.e. input and output ports. Since some portion of the power is absorbed by scatterer and some portion of it is scattered in upward and downward directions, power conservation is not applied when this system is modeled with two ports. In fact, scattering matrix of such system will not be unitary matrix. By using a and b coefficients, we proposed the way to calculate S-parameters of single scatterer which is given as follows:

$$S_{11} = \frac{b_i}{a_i} \times e^{2(-j\beta+\alpha)L_i} \tag{5.15}$$

$$S_{21} = \frac{a_0}{a_i} \times e^{(-j\beta+\alpha)(L_i+L_o)} \tag{5.16}$$

$$S_{12} = S_{21} \tag{5.17}$$

$$S_{22} = S_{11} \tag{5.18}$$

Here, for the calculation of S_{11} and S_{21}, S-parameters are multiplied with exponential factor which is basically phase and attenuation correction. There β and α represents real and imaginary part of wavenumber which belong to fundamental mode. By doing that, we effectively carried input and output planes to the scatterer's location and the

effect originated by propagation before reaching expansion planes are removed. Due to reciprocity and symmetry of the system, S_{12} and S_{22} are found easily.

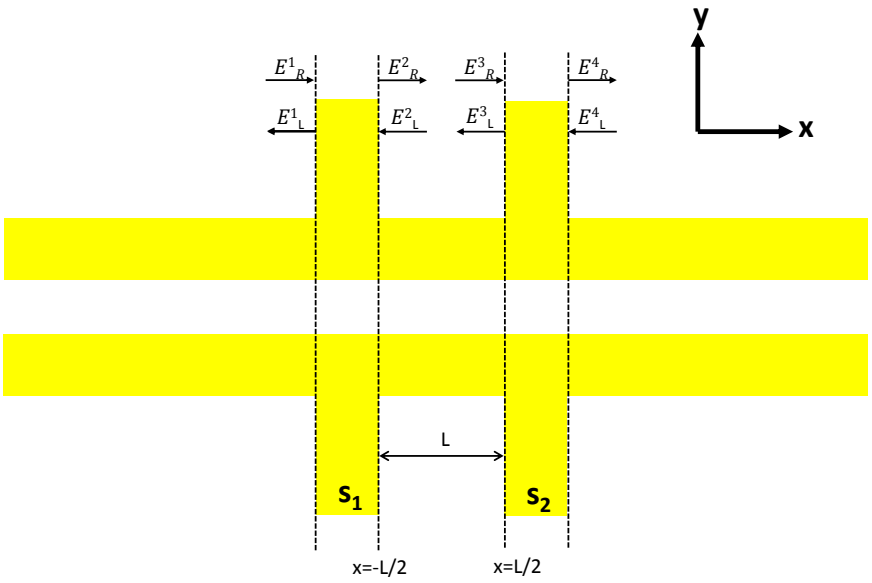

Figure 5.4: Two identical antennas seperated by L. The mode amplitudes before and after each scatterer are shown with E. Subscript R indicates that field is propagating to right,whereas L indicates that mode is propagating to left.

Two elements array of dipole antennas which are separated by distance L is shown in the Figure 5.4. Now, we are at the point that we can model such cascaded array of antenna scatterers. Since we already found scattering matrix of single antenna, it can be transformed into transfer matrix. For the region in between scatterers, transfer matrix representation is also needed and it can be calculated by accounting the phase accumulation of the propagating guided mode in the middle region. Transfer matrix of propagation of distance L is shown below.

$$\mathbf{T}_p = \begin{bmatrix} e^{(j\beta-\alpha)L} & 0 \\ 0 & e^{(-j\beta+\alpha)L} \end{bmatrix}$$

Then, by multiplying transfer matrix of each element, overall transfer matrix can be

obtained easily as follows where $\mathbf{T_1}$ and $\mathbf{T_2}$ represents transfer matrix of scatterer 1 (s_1) and scatterer 2 (s_2).

$$\mathbf{T}_t = \mathbf{T}_1 \mathbf{T}_p \mathbf{T}_2 \tag{5.19}$$

Finding overall transfer matrix allows us to calculate amplitude transmission(t) and reflection(r) coefficients directly from resulting matrix elements. They can be written in terms of elements of overall transmission matrix as follows

$$r = -\frac{T_{21}}{T_{22}} \qquad t = T_{11} - \frac{T_{21}T_{12}}{T_{22}} \tag{5.20}$$

Transmitted and reflected power intensities can be found by taking absolute square of amplitude coefficients.

5.2.1 Transmission and Reflection

Embedded antennas can be placed as an array in the waveguide with controlled separation in the propagation axis as in 5.4. Since they act as partial reflectors, reflected waves will be constructively or destructively interfere with the incoming guided wave, hence reflection can be increased or decreased in the chosen wavelength. Although major purpose of this study is not manipulating reflection or transmission of arrayed antennas, we will use transmission and reflection results to test our model.

We applied our formalism to model dipole antennas embedded in plasmonic two wire transmission line waveguides (TWTL). Waveguide gap and metal thickness are set to 50 nm. Metal lines of width 75 nm are used. Wavelength dependent gold permittivities are taken from the literature [25]. Waveguide is surrounded by air as substrate and superstrate for simplicity. FDTD simulations are performed with commercial Lumerical

FDTD solver. Mesh size is set to 5 nm in the vicinity of the waveguide and antennas. PML boundaries are placed in all planes. We first tested our formalism by comparing transmission and reflection results found by Lumerical with results predicted by our S-matrix approach. To do that, first we placed a single antenna (Design S1) shown in Figure 4.7a, which is resonant around $\lambda = 1.55$ μm. S-parameters of this antenna are found by using the method explained in the Figure 5.3. Then, its S-matrix is transformed into its transfer matrix, then for various L separations, total transfer matrix is calculated for the two antenna array. For transmission measurements, input and output ports are defined at the point where scatterer array starts and ends, respectively . For reflection measurements, they are defined at the point where scatterer array starts. In fact, definition of input and output ports can be made arbitrarily which will not change any results. However, to discard attenuation effects, so to see the effect of array more clearly, such arrangement is used. Transmission and reflection is measured in Lumerical by placing power monitors at the cross section of waveguide. We kept the size of power monitors as 800 nm in y axis and 400 nm in z axis not to be affected from unguided scattering light. Later, we also confirmed the assumption made at the beginning by expanding the fundamental mode at the location of these monitors to make sure that recorded power belongs to the fundamental mode only.

Figure 5.5 shows transmitted power intensities of various L in the wavelength range of 1-3.5 μm. FDTD results are shown with black curve and the results calculated by S-matrix approach is shown with red curve. For wavelengths not in the vicinity of resonance, two curves perfectly fit. Around the resonance, predicted location of the transmission dip and its numerical value are very close to results simulated by FDTD.

Same formalism is also applied to find reflected wave intensities. As seen in Figure 5.6, for separations of L=600 nm and L=1000 nm, FDTD and S-matrix curves perfectly overlaps for frequencies not in close vicinity of antenna resonance. Peak and dip lo-

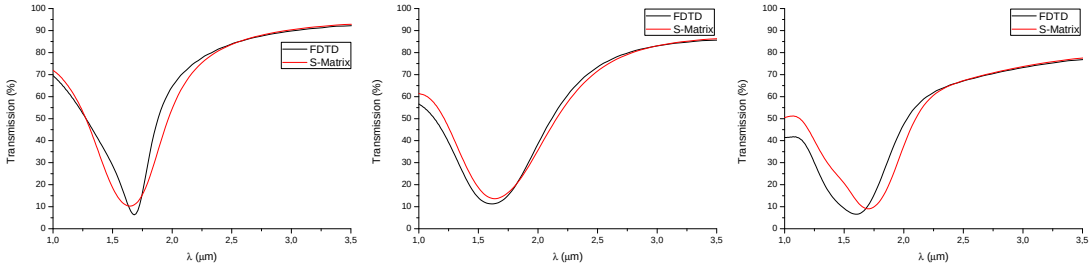

(a) L=200 nm (b) L=600 nm (c) L=1000 nm

Figure 5.5: Comparison of transmission values of FDTD result and S-Matrix prediction for 2 antenna array separated by distances 200 nm, 600 nm, 1000 nm. Input and output ports are defined as just before the first antenna and just after to the second antenna, respectively.

cations are also very closely predicted in the whole wavelength range. Although peak intensities are not exactly same for both curves (around the resonance), still general behavior is well predicted by using our method. Since discrepancies are only distinct around resonances, we predict that, due to strong scattering at resonance, some extra channels are created that increase reflection. On the other hand, for the separation of L=200 nm, discrepancies are more significant, though we are able to predict dip and and peak locations very successfully. As the separation decreases further than L=200, S-matrix results become less relevant to actual result, so this difference is explained with near field effects which become more significant when antennas are closely located to each other.

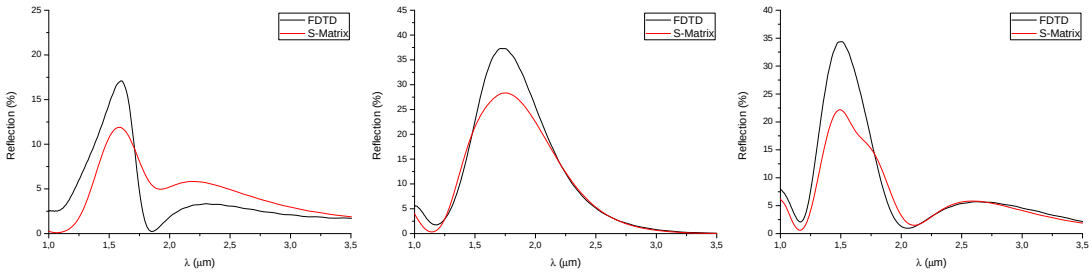

(a) L=200 nm (b) L=600 nm (c) L=1000 nm

Figure 5.6: Comparison of reflection values of FDTD result and S-Matrix prediction for 2 antenna array seperated by distances 200 nm, 600 nm, 1000 nm. Input and output ports are defined at the entrance of first antenna.

Transmission and reflection analyses show that S-matrix formalism is successful on predicting general shape of transmission and reflection curves, even with their numerical values in the broad range of wavelengths. Therefore, we can proceed with our approach to further model radiation characteristics of antenna arrays.

5.2.2 Outcoupling and Beam Steering

As in radio-frequency, we predict that nano antenna arrays embedded in plasmonic waveguide can be used to control the angle of radiation. To achieve that, one should change the antenna separation, so due to the propagation phase and the attenuation of guided mode, varying L will change excitation amplitudes and phases of antenna array elements. Therefore, our prediction is that by playing with L, angle of radiation can be controllable.

To support our idea, we investigated angular distribution of out coupled light from the single antenna and two antenna elements separated by different L. The geometry of waveguide and simulation parameters are chosen as in the transmission and reflection simulations. We excited the fundamental mode of the waveguide to drive antennas. A wide field monitor is placed at 200 nm above antennas (xy plane) to record radiated near fields. Later, near-to-far field projection is performed with Lumerical FDTD to see the angular distribution of radiated light in the upper xy plane. Figure 5.8a shows angular $|E|^2$ distribution of radiated light calculated for $\lambda = 1.55$ μm. θ is defined as the angle with respect to xy plane and ϕ is defined as the angle with respect to xz plane. Inner circles that are shown in figures represents θ and straight lines shows various ϕ directions. The figure in the middle belongs to the single antenna which heavily radiates in the perpendicular direction to the xy plane ($\theta = 90°$). The one at the left is showing result of two antennas separated by L=400 and right one shows the result for L=800.

The main beam angle of the first one is around $\theta = 60°$ whereas third one radiates mainly around at $\theta = 110°$. Our prediction regarding array effect is clearly visible in this figure, so as L changes, the direction of maximum radiation changes in θ.

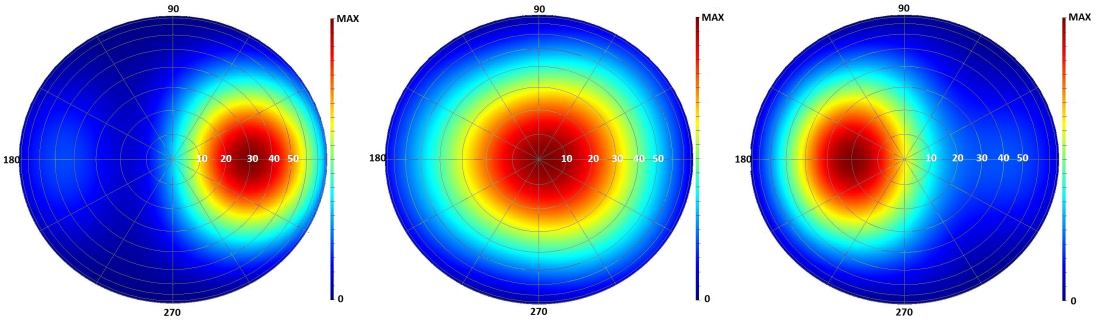

(a) L=400 nm (b) Single Antenna (c) L=800 nm

Figure 5.7: Comparison of angle dependent radiated field intensities ($|E|^2$) on the upper hemisphere which has radius 1 m (far field projected) at $\lambda = 1.55\ \mu m$. Near field monitor 200 nm above structures (xy plane) projected to the far field to see angular distribution of radiated (out coupled) light for different geometries: single antenna, double antennas with L=400 nm and L=800 nm.

Now we turn our attention to modeling of this effect. After finding total transmission matrix of antenna arrays with separation L, by using the following relation, one can get amplitudes of right and left propagating modes, at defined ports shown in the Figure 5.4. E_R^1 represents the input beam and it is taken as unit amplitude 1, so other components are normalized with respect to input.

$$\begin{bmatrix} E_R^1 \\ E_L^1 \end{bmatrix} = \begin{bmatrix} 1 \\ t \end{bmatrix}; \qquad \begin{bmatrix} E_R^2 \\ E_L^2 \end{bmatrix} = \mathbf{T}_1 \begin{bmatrix} E_R^1 \\ E_L^1 \end{bmatrix}; \qquad \begin{bmatrix} E_R^3 \\ E_L^3 \end{bmatrix} = \mathbf{T}_p \begin{bmatrix} E_R^2 \\ E_L^2 \end{bmatrix}; \qquad \begin{bmatrix} E_R^4 \\ E_L^4 \end{bmatrix} = \mathbf{T}_3 \begin{bmatrix} E_R^3 \\ E_L^3 \end{bmatrix}$$

After finding mode amplitudes, we calculated antenna excitations s_1 and s_2 as in Equation 5.21 and 5.22. Only fields propagating towards to antennas are taken as input, since all normalizations are done with respect to single antenna for which we assumed s=1. Therefore, s_1 is found by adding amplitudes of fields propagating to the left and

to the right, towards first antenna. For the calculation of s_2, only the mode propagating to the right is taken into account since it is assumed that there is no reflected fields coming from the right end of the waveguide.

$$s_1 = E_R^1 + E_L^2 \tag{5.21}$$

$$s_2 = E_R^3 \tag{5.22}$$

Then array factor is found by using Equation 5.9, and radiation pattern is calculated by using Equation 5.5. We calculated element factor of single antenna by using FDTD simulations that we showed in the Figure 5.7b. Figure 5.8a compares FDTD results with our model's prediction. As seen, peak position (maximum radiation angle) is determined almost correctly, that proves the accuracy of our model. Although, the peak at the left is over-guessed compared to actual FDTD result, that will not be changing coupling efficiency results much since major beam direction and its distribution are predicted quite well.

Total radiated power in all angles and wavelengths, then, can be calculated by using 5.6 and radiated power of single antenna (element factor) which is found by FDTD simulations. FDTD results and our predicted coupling efficiency calculations are compared for L=800 nm with varying λ. In Figure 5.8b, general behavior of coupling efficiency vs λ curve is well predicted, that shows that our proposed model works with accuracy.

Our model is proven to be successful to analyze antenna arrays embedded in waveguides and predict the radiated power and its angular distribution. Now, we can use our model to show the effect of the separation on the angle of maximum radiation (direction of main beam) and coupling efficiencies. Following figures are calculated for two antennas by keeping the wavelength as constant at $\lambda = 1.55$ μm. Effect of antenna seperation (L) is clearly seen in Figure 5.9a where direction of maximum radiation gradually changes

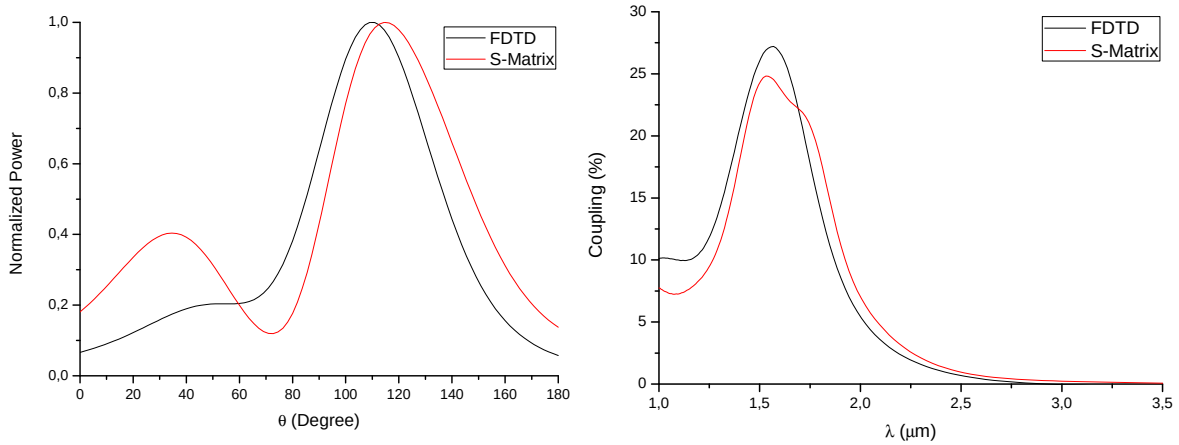

(a) Normalized power vs θ at $\lambda = 1.55\ \mu m$ and L=800 nm

(b) Coupling efficiency vs λ for array of two antennas with L=800 nm

Figure 5.8: Comparison of FDTD and semi analytical s-matrix results in terms of radiation properties.

between $\theta = 120°$ and $\theta = 60°$. Also, total coupling efficiency (Figure 5.9b) displays a sinusoidal variation which can be explained by Fabry-Perot resonance like behavior of the two antenna system that causes periodic change in excitation amplitudes.

To sum up, antennas embedded in the plasmonic waveguide behave as antenna arrays, so their radiation characteristics are controllable by varying their separation. Our model shows that S-matrix and antenna array formalism can be applied to them to predict their behavior. Therefore, this configuration is more promising than previous studies where antennas are placed at the opening of waveguides, since it allows us to control and predict both direction and total radiated power. Although we predict that the formalism that worked for two antennas can be applied to arrays with more number of elements, we were unable to predict the behavior of three element arrays.

Until now, we have only shown a sample structure that is cladded by air, but same formalism can be applied to structures where waveguides and antennas are located on a substrate. We only considered one type of antenna, dipole like antenna with two arms, but same model can be extended to other antenna types such as bow-tie antennas or

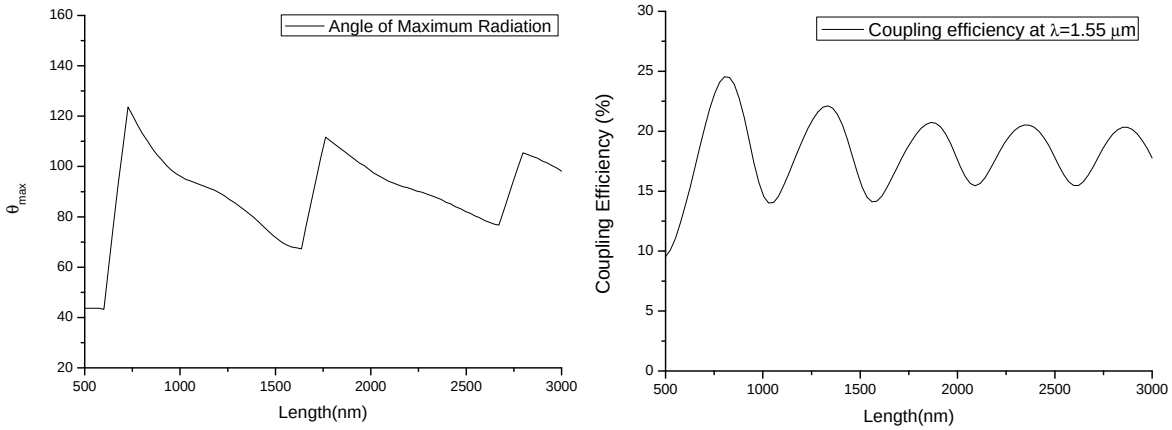

(a) The effect of antenna separation (L) on the maximum angle of radiation

(b) The effect of antenna separation (L) on the total coupling efficiency

Figure 5.9: The effect of antenna separation(L) of two antenna system on the radiation characteristics. The $\lambda = 1.55\ \mu m$ is fixed and θ_{max} and coupling efficiency are calculated by employing S-matrix approach

even arbitrary scatterers.

5.2.3 Smart Coupler Design

Here we will show a sample design of efficient antenna coupler by using the developed antenna array formalism. Figure 5.9b shows coupling efficiency (from the waveguide to free space) with respect to antenna separation predicted by our model. As seen, L=800 nm exhibits quite efficient coupling which reaches around 25%. So we will use antenna separation of L=800 nm as a starting point for FDTD simulations. Figure 5.10b shows top view of designed 2-element antenna and I/O plane. For the calculation of coupling efficiency from waveguide mode to the free space, fundamental mode of the waveguide is sent from I/O plane and power is collected at the upper half plane. Then, input port is defined as the beginning point of the left antenna and normalization with respect to the input power is done. For the calculation of coupling efficiency to the waveguide, a Gaussian beam with waist diameter=1.2 μm which is centered in the center of scatterer configuration and focused on the plane 200 nm above antennas is incidentally sent

from the upper plane (y-polarized). Then power is recorded in the waveguide mode on the I/O plane and it is projected back to the beginning of first antenna to discard attenuation effects. Then normalization is done with respect to total power in the input Gaussian beam. Figure 5.10a shows both coupling efficiencies found by using FDTD simulations. As seen, from the waveguide to free space coupling reaches values above 25% at $\lambda = 1.55$ μm. Moreover, from Gaussian beam to mode coupling efficiency also reaches around 15%. Since the system is symmetric and Gaussian beam is located at the center of x-axis, left and right propagating modes are equal in power. Hence, Gaussian is coupled to both left and right propagating modes of the waveguide with equal strength.

Figure 5.9a shows maximum angular radiation direction predicted by our model. As seen, for L=800 nm, maximum radiation is in the direction of $\theta = 112°$, but when we couple from Gaussian beam to the waveguide, we send the beam parallel to the antenna surface normal ($\theta = 90°$). To better couple from Gaussian beam to waveguide, angled Gaussian beam from the direction of maximum radiation is sent to the antenna array. For this configuration, coupling is enhanced to 23% which is more close the coupling efficiency value found for waveguide to free space case. This is expected since for this case, we have better spatial matching between sent Gaussian beam and radiated beam when the mode is sent from the waveguide.

The coupling efficiencies can be further enhanced by blocking the right propagating channel of the waveguide. For this purpose, a reflector shown in 4.7c are employed. The reflector is located at d=400 nm to the right of the right antenna. Then simulations are performed by following the same procedure with the previous geometry. Figure 5.11a shows clear enhancement of coupling efficiencies for both configurations. Coupling efficiency to free space is reached to 30 % and coupling efficiency to the WG is reached to 22% by blocking the right channel of the waveguide since the mode that leaks to the right port is inhibited with this design. We also sent the Gaussian beam in the direction

of maximum radiation similar to previous case, for that configuration coupling efficiency increased to 28%.

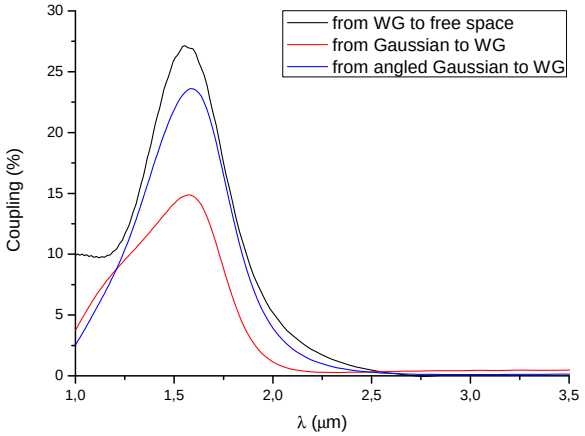

(a) Coupling efficiencies for geometry in Figure 5.10b. Black curve shows the coupling efficiency from the waveguide mode to the free space. Red curve shows coupling efficiency from Gaussian beam to the waveguide mode. Blue curve shows coupling efficiency from angled Gaussian beam ($\theta = 112°$) to the waveguide mode.

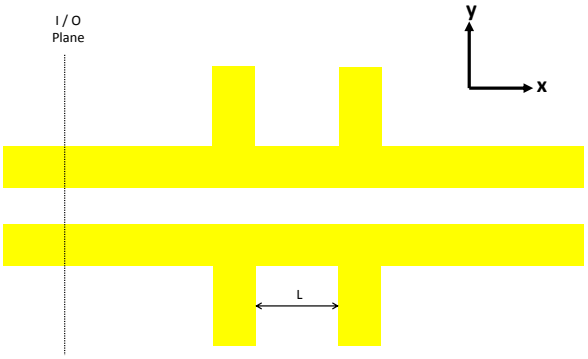

(b) Top view of 2-elements antenna array.

Figure 5.10: Coupling efficiencies of 2-antenna geometry and top view of the coupler.

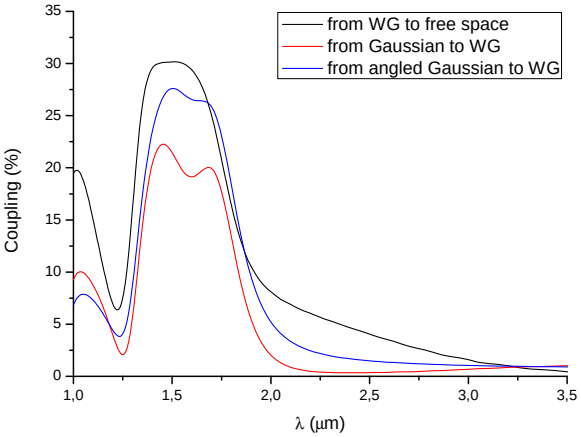

(a) Coupling efficiencies for geometry in Figure 5.11b. Black curve shows the coupling efficiency from the waveguide mode to the free space. Red curve shows coupling efficiency from Gaussian beam to the waveguide mode. Blue curve shows coupling efficiency from angled Gaussian beam ($\theta = 112°$) to the waveguide mode.

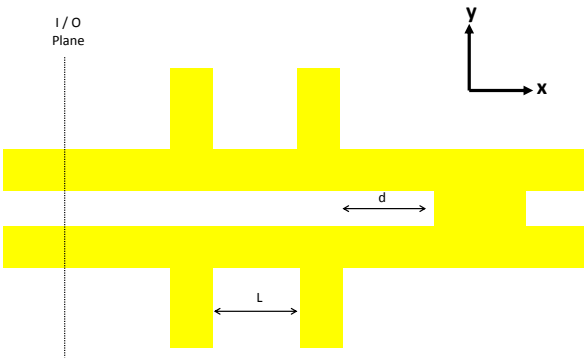

(b) Top view of 2-elements antenna array and reflector that blocks right channel of the waveguide.

Figure 5.11: Coupling efficiencies of 2-antenna geometry with a reflector and top view of the coupler.

Chapter 6

Fabrication and Optical Measurements

In the third and fourth chapters, we introduced sub-wavelength three dimensional plasmonic waveguides and sample antenna coupler designs for them. For the frequency range of interest, designed components are sub-micron in size, hence fabrication of such structures requires special attention. Fortunately, for the fabrication of micrometer scale structures, there are mature technologies such as optical lithography and etching, and they are widely used in today's microelectronics industry. On the other hand, sub-micron components that we are interested in are much smaller than micrometer, i.e. designed slot waveguides have gap of 50 nm. Therefore, one should employ state-of-art methods known as nanofabrication in general for the fabrication of such delicate designs. In fact, we are able to fabricate slot waveguides with gaps around 40 nm by using methods exists in the literature.

One of the critical step of fabrication process is called nanolithography. Nanolithography is a patterning technique to transfer pre-designed geometrical patterns into the sample or a chemical material layer on the sample. There are many known nanolithography methods such as optical lithography, electron-beam lithography (EBL), focused ion beam lithography (FIB), nano-imprint lithography etc. Each of these techniques has some advantages over others which depends on the application. Among them, EBL and FIB are direct-write methods that do not require initial step of writing masks. Hence, those methods are more appropriate for low-volume applications instead of mass production. We used EBL as a lithography technique in our fabrication process whose

details will be explained later.

We started the fabrication process with silicon wafers, after realizing that slot modes do no exist if silicon is used as substrate, we switched to $Si/Si0_2$ (500 nm) and quartz wafers. Two different process lines are completed. Details of each process step and substrate-dependent differences will be explained below. Here, only general procedures that are followed will be given. Full fabrication recipe can be found in the Appendix: Fabrication Recipe.

6.1 Dicing

We started the process with 100 mm diameter p-doped silicon substrate with 500 nm thermally grown oxide on it. Total thickness of the wafer is 500 µm and silicon is single crystal with $\langle 100 \rangle$ orientation. Thanks to its crystal nature, this wafer can be diced easily by scratching it with a diamond-pen. We have diced the full wafer into 2 cm $\times$ 2 cm samples. Second type wafer used for fabrication is quartz with 500 µm thickness. Unlike silicon, quartz wafers are hard to handle and to dice with diamond-pen. Hence, we used automatic DISCO DAD 320 dicing system to dice it to 2 cm $\times$ 2 cm. Before dicing, quartz wafer is coated with thick optical resist to avoid any damage during dicing. Later, in the cleaning step, coated resist is cleaned.

6.2 Cleaning

After dicing, samples are cleaned to get rid of any organic contaminants or residues by using standard piranha cleaning procedure. Piranha solution is mixture of hydrogen of peroxide (H_2O_2) and sulfuric acid (H_2SO_4). The ratio of compounds depends on the protocol. We have used one of the most common mixture which has H_2SO_4 (3) :

(1) H_2O_2. It is a solution that reacts exothermically and it can reach to very high temperatures when they are reacted. Hence, this acid solution should be handled with special attention. We placed our samples carefully to petri dish which has recently mixed piranha solution and left them for a few ten minutes. After solution's temperature goes down, they are taken out and rinsed with DI water in three different beakers consecutively. Then, cleaned samples are dried by using N_2 gun.

6.3 Electron Beam Lithography

PMMA (polymethyl methacrylate) is a polymer used as positive resist for e-beam lithography. There are two standard PMMA-based products available in the market with different molecular weights. The thickness of PMMA coating is determined by the molecular weight and spinning rate of coating. Hence, to coat samples with 100 nm thick polymer, we used PMMA 950 A2 obtained from MicroChem Corp. Cleaned samples are spin coated at 1600 rpm as a pre-step of EBL process. Later, coated samples are baked in the hot plate which made them ready for EBL patterning.

Resist coated samples are patterned with Vistec EBPG 5000+ (100keV) EBL system. Here it is important to note that the most critical step of EBL process is deciding on correct patterning parameters for achieving desired patterns as end result. That's why we patterned same geometries by using different dosage and current values to decide on the most appropriate process parameters. The dose values higher than the correct dosage is called overdose, and it might result in exposure of unnecessary regions on the chip. Also the spots that is surrounded by exposed area can be overdosed due to proximity effect - higher exposure due to scattered electrons. Very high doses also cause distortions such as fattening in outer boundaries of closed rectangles. A clear example of overdose is seen in the fabrication of gaps of our slot waveguides. Since exposed

regions will be coated with metals at the end of fabrication, overdose might result in loosing gaps between metallic pads. Figure 6.1 shows such a result in which rectangles at sides of the slot waveguide are overdosed and as a result the gap is unintentionally exposed. In Figure 6.1a, a clear gap is seen (correct dose) whereas as in figure 6.1b gap disappeared (overdose).

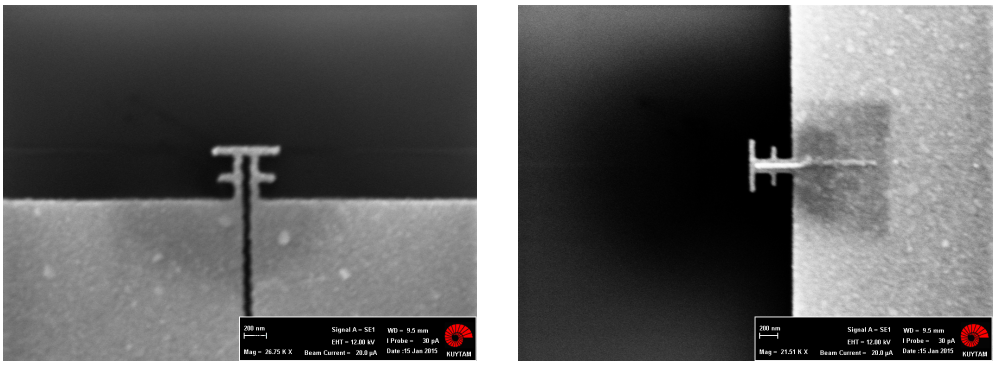

(a) Dose is correct (b) Overdose

Figure 6.1: SEM images of fabricated slot waveguides, correct and overdose examples.

EBL technique is basically writing geometrical patterns with electrons to the resist. In this method, sample is heavily bombarded with electrons, and electrons leave the substrate after reacting with resist chemically. However, for insulating substrates electrons accumulate on the substrate since there is no pathway to be neutralized. Hence, for such substrates, charged surface cause the deflection of incoming electron beam which eventually decreases the resolution of the system. Quartz is an example of such insulating substrate, therefore one should find a way to avoid charging effect. To handle this problem, we thermally coated our substrate with thin 10 nm Aluminum after resist coating. By this way, Aluminum layer acts as a conducting layer which creates conductive path for accumulated electrons. Then we performed patterning. Later, Al layer is removed by dipping it to the TMAH based photoresist developer AZ-726 MIF for 1 minute. This extra step was successful to avoid the problems caused by charging.

Patterned samples are then developed by MIBK and IPA mixture. The ratio of two

directly changes sensitivity and resolution. Two commonly used recipes are 1:3 and 1:1, former has higher resolution and lower sensitivity and latter has lower resolution and higher sensitivity compared to each other. Hence, it is expected to see that correct dosage is low for the second one due to increased sensitivity. We tried both ratios before finalizing our process recipe and observed the effects. The recipe details are shown in the Appendix: Fabrication Recipe.

6.4 Thermal Evaporation

After developing samples, we first deposited 5 nm thick titanium as an adhesive layer. Then 40 nm thick gold is deposited. Both deposition is done by using Nanovak NVTS thermal deposition system. In the first run, Ti and Au are deposited with rates 0.2 A/s and 1.5 A/s, respectively. After inspection of these samples with SEM, we concluded that metal surfaces are rough due to high deposition rate. In the next run, deposition rate for both Ti and Au are lowered to 0.2 A/s . This solved the roughness problem, as seen in Figure 6.2 where differences on smoothness of metallic pads seen clearly.

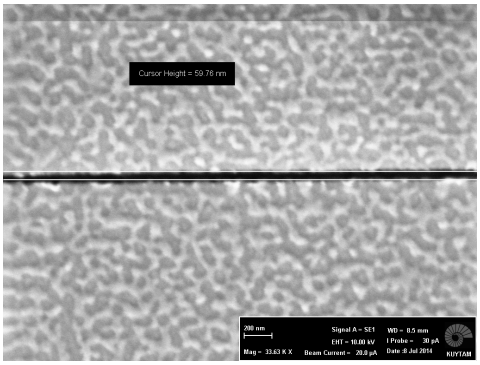

(a) Metals deposited with higher rate have rough surface

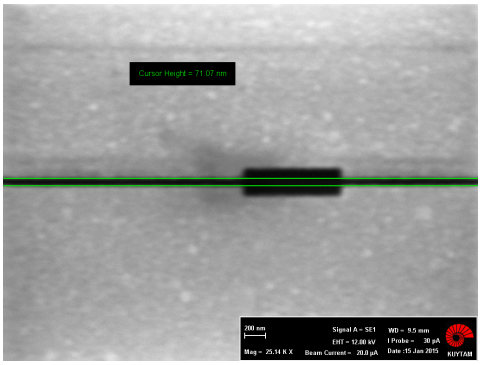

(b) Metals deposited with slower rate have smoother surface

Figure 6.2: SEM images of metal pads deposited by different rates.

6.5 Lift-off

After metal deposition, samples are put in the hot acetone for 10 minutes. Then we rinsed them with acetone flush without allowing them to dry. Later, they are put to acetone and IPA in sequence and they are kept in the ultrasonic bath for 10 minutes. The thickness of metal and resist thickness are important parameters that have to be chosen carefully for successful lift-off process. Since the resist that we used has thickness around 100 nm, we did not deposit metals thicker than 50 nm not to cause any liftoff problem. Keeping the ratio of metal thickness to resist thickness smaller than 1/2 is important not to loose resolution of structures. However, still in some samples we faced lift-off problems as seen in Figure 6.3.

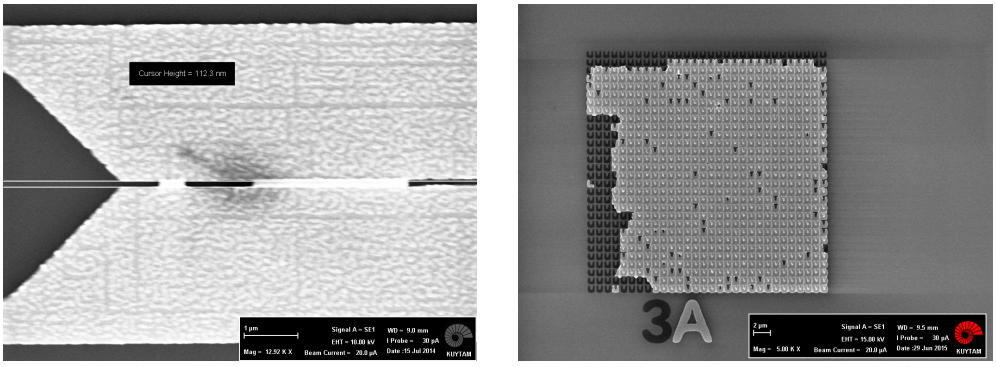

(a) Undesired metal stays in gaps due to lift-off problem

(b) A sample with a major lift-off problem

Figure 6.3: SEM images of structures that have lift-off problems

In Figure 6.4, we show SEM images of successfully fabricated plasmonic slot waveguides with input and output antenna couplers placed at openings. The gold thickness is 40 nm and gap size is 50 nm, quartz is used as substrate.

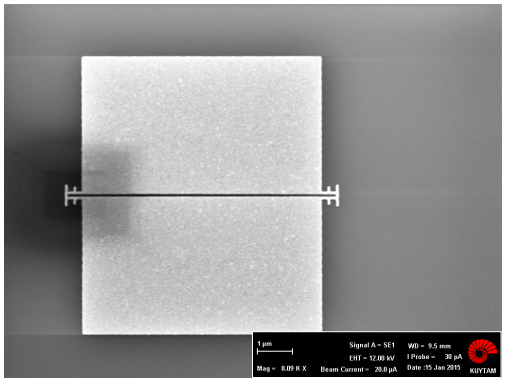

(a) Flat plasmonic slot waveguide with input/output antenna couplers

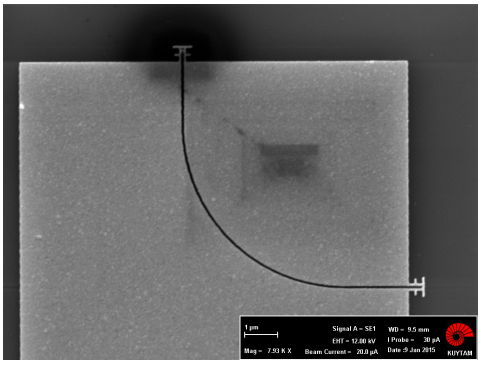

(b) Bended plasmonic slot waveguide with input/output antenna couplers

Figure 6.4: SEM images of successfully fabricated plasmonic waveguides and antenna couplers, on quartz substrate. Gold thickness is 40 nm and gap size is 50 nm.

6.6 Optical Setup

An optical setup is designed to characterize fabricated plasmonic waveguides, and to measure their coupling efficiencies. Schematic diagram of the setup is shown in the Figure 6.5. Broadband supercontinuum laser is used as the light source which is connected to output channels NIR1 and NIR2 after filtered by the acousto optic tunable filter (AOTF). Two optical paths are combined by using mirrors, where flip mirror allows us to choose between two output channels. We placed an ND filter to block some portion of the incoming power, in the case of less power is required. Irises (two of them are on the vertical, one is on the horizontal path) are used to align the optical path. The polarization of laser is controlled by half-wave plate (HWP) and first polarizer which is located just before HWP. Then, laser light is focused on the sample by using an objective lens (Leica,100x ,NA0.9). High numerical aperture is intentionally chosen to decrease the waist size of the laser beam and to effectively collect out the coupled light from waveguides. XYZ piezo stage is employed to focus the laser and to accurately position the sample in the XY plane. The collected light by the objective is directed to the horizontal path by using a 50:50 beam splitter(BS). A polarizer is used after

BS, to only collect out coupled light of the desired polarization. Waveguides of Figure 6.4b are designed as bended to decrease noise. Since input and output polarization are 90 degree shifted, with the help of second polarizer, it is possible to block unwanted polarization component including direct reflections [17]. We also put additional lens f2 to have an image plane where we can block light coming from input of the waveguide. By appropriately placing and narrowing the gradual iris in front of the image plane, we guaranteed that only the data coming from output of the waveguide is allowed to reach detector. For the, alignment of beam and samples, an IR camera is used with zoom lens f4. LED light is also added to the beam path with BS to illuminate the sample during the alignment. After, appropriately placing input beam on the input coupler of the waveguide and and setting the location of iris blockage as not to allow input beam, the data is collected by IR detector. The proposed optical setup is built and aligned, and we are able to see clear images of fabricated structures by using IR camera. The next step is measuring the coupling efficiencies by methods proposed in this section.

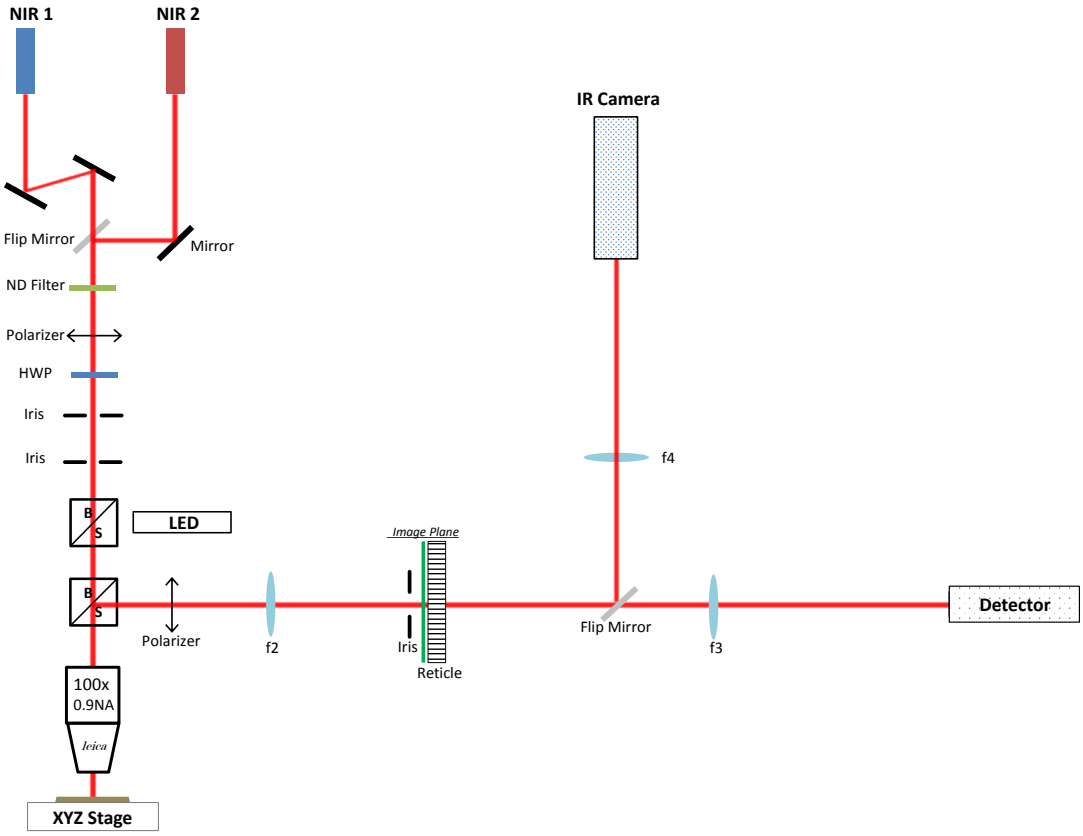

Figure 6.5: Schematic of optical setup to measure properties of plasmonic waveguides.

Chapter 7

Conclusion and Future Work

Breakthrough innovations and developments that we enjoyed in the 20th and 21st centuries were made possible by electronics, particularly highly integrated circuits that are capable of processing massive amount of data in a limited space and time. However, as they become denser and faster, limits of them are started to be visible in the horizon. Increased resistance and capacitance effects due to longer metallic connections, densely packaged transistors which produce extraordinary amount of heat and fabrication limitations of smaller transistors are a few examples of problems that are emerged. Since, clock speeds of circuits are limited due to mentioned effects, current trend is using multi-core processors and clusters that utilize multiple computers. However, they are not full solutions, since the communication speed between chips is also a limiting factor. Therefore, utilizing optics is vital to overcome bottlenecks of electronics. Plasmonic seems a promising solution due to its compactness and integrability with electronics. Plasmonic waveguides can be used to transfer the data between components of electronics on a chip, or more excitingly they can be used to build optical processors that process information much faster than electronic counterparts.

In spite of apparent potential of plasmonic waveguides to use in future data transmission, there are still questions to be answered and problems to be solved such as designing efficient couplers between waveguides or between free space and plasmonic waveguides. One promising solution of this problem is placing scatterers such as resonant antennas to the end openings of sub-wavelength plasmonic waveguides, however they are hard to

design and complicated to model. Also, in the opposite way, from waveguide to free space coupling, the direction of radiation is not very controllable for such designs, at least not with a systematic way.

In this study, we proposed and proved a promising solution to the efficient coupling and directive radiation problem by adopting antenna array concept existing in radio-frequency. Before developing the solution, the mode properties of plasmonic slot and two wire transmission line waveguides (TWTLs) were studied. The dispersion relation of each geometry, substrate effects, the relation between dispersion relation and metal thickness, gap and width were investigated in detail. Then, an antenna design to couple light from the free space to the plasmonic slot waveguide was shown. At the same chapter, various scatterer geometries were studied by comparison, we found that some of geometries act as good reflector and some of them were good radiators. In the modeling chapter, first, tools such as S-matrix and array concepts were introduced. Later, by using these tools and scatterer designs made in previous chapter, a semi-analytical method was developed to model transmission, reflection and radiation characteristics of arrayed embedded antennas. We successfully showed that these arrays can be used and systematically designed to control the angular direction of radiated beam. Also it was shown that our method is very good at predicting coupling efficiencies and angular distribution of radiating antenna arrays. Later, we showed a sample design that couples light from waveguide to the free space and from Gaussian beam to the waveguide mode. In the last chapter, we outlined fabrication steps of sub-wavelength nano structures that work in the near infrared region. Finally, the schematic of optical setup to experimentally characterize these structures was illustrated.

Although we did modeling analysis only for metal films hanged in air, same methodology can be applied to geometries where substrate is a dielectric. These designs can be experimentally studied by measuring angular radiation properties to further confirm

our predictions. Also various other scatterers, such as non-resonant antennas and bow-tie antennas can be embedded in the waveguide. In fact, there might be other designs that offer better solutions to the coupling problem. Another exciting application might be phase controlled antenna array. For instance, channel of the waveguide can be filled with electro-optic material [66], and direction of out coupled light might be modulated by external electronics by electro-optically varying refractive index of gap material.

Appendix A

Fabrication Recipe

1. Dicing
    - Coat wafer with thick photo resist
    - Place wafer on UV sensitive tape
    - Dice wafer with DISCO DAD 320 system into 1.5 cm sided squares
    - 5 mins UV exposure with Mask Aligner
2. Cleaning
    - Mix 95% H_2SO_4 (50 mL) with 35% H_2O_2 (20 mL), always put acid first
    - Wait for 2 minutes to cool down
    - Keep samples in piranha mixture for 5 mins
    - Wash samples with DI Water 1 for 30 seconds
    - Wash samples with DI Water 2 for 30 seconds
    - Wash samples with DI Water 3 for 30 seconds
    - Dry samples with N_2 gun
3. Resist Coating
    - Use 950 PMMA A2 (MicroChem Corp.) positive e-beam resist
    - Step 1: 500 rpm for 4 seconds

- Step 2: 1600 rpm for 45 seconds
- Step 3: 0 rpm for 3 seconds
- Post-bake at 170 °C for 5 mins

4. Conductive Layer Coating
    - This step is only for quartz wafers
    - Coat with 10 nm Aluminum with thermal evaporation
    - Rate is 0.5 Å per second
    - Remove metal layer after EBL step by dipping sample to AZ 726 MIF for 60 seconds
5. Electron Beam Lithography
    - Vistec EBPG 5000+ EBL sytem is used
    - Place samples to sample holder
    - Adjust the angle of sample with laser stage
    - Record coordinates of corners to find center of the sample
    - Load samples to the device
    - Make a dose array for doses around 1000 $\mu C/cm^2$
6. Developing
    - 1:3 (MIBK:IPA) for 60 seconds
    - 1:1 (MIBK:IPA) for 10 seconds
    - Stop developing by dipping it to IPA
    - Dry with N_2 gun

7. Metalization

    - NANOVAK NVTS-400 thermal evaporator is used
    - Put samples into vacuum, base pressure is 3e-7 Torr
    - 5 nm Ti with rate 0.2 Å/ second
    - 40 nm Au with rate 0.5 Å/ second

8. Lift-off

    - 10 mins in hot acetone (50 °C)
    - Rinse with acetone
    - 10 mins in acetone with ultrasonic cleaner
    - 10 mins in IPA with ultrasonic cleaner
    - Dry with N_2 gun

Bibliography

[1] W. F. Brinkman, D. E. Haggan, and W. W. Troutman, "A history of the invention of the transistor and where it will lead us," *IEEE Journal of Solid-State Circuits*, vol. 32, no. 12, pp. 1858–1864, 1997. 1

[2] R. R. Schaller, "Moore's law: past, present, and future," *IEEE Spectrum*, vol. 34, pp. 52–55, 57, June 1997. 1

[3] I. L. Markov, "Limits on fundamental limits to computation," *Nature*, vol. 512, pp. 147–154, Aug. 2014. 1

[4] B. E. Little and S. T. Chu, "Toward Very Large-Scale Integrated Photonics," *Optics and Photonics News*, vol. 11, p. 24, Nov. 2000. 1

[5] R. Nagarajan, C. Joyner, J. Schneider, R.P., J. Bostak, T. Butrie, A. Dentai, V. Dominic, P. Evans, M. Kato, M. Kauffman, D. Lambert, S. Mathis, A. Mathur, R. Miles, M. Mitchell, M. Missey, S. Murthy, A. Nilsson, F. Peters, S. Pennypacker, J. Pleumeekers, R. Salvatore, R. Schlenker, R. Taylor, H.-S. T. H.-S. Tsai, M. V. Leeuwen, J. Webjorn, M. Ziari, D. Perkins, J. Singh, S. Grubb, M. Reffle, D. Mehuys, F. Kish, and D. Welch, "Large-scale photonic integrated circuits," *IEEE Journal of Selected Topics in Quantum Electronics*, vol. 11, pp. 50–65, Jan. 2005. 1

[6] Intel, "The 50g silicon photonics link," tech. rep., Intel Corporation, 2010. 1

[7] K. Aydin, "Integrated optics: Nanostructured silicon success," *Nature Photonics*, vol. 9, pp. 353–355, May 2015. 2

[8] N. Liu, M. Mesch, T. Weiss, M. Hentschel, and H. Giessen, "Infrared perfect absorber and its application as plasmonic sensor," *Nano Letters*, vol. 10, pp. 2342–2348, July 2010. 2

[9] H. Im, H. Shao, Y. I. Park, V. M. Peterson, C. M. Castro, R. Weissleder, and H. Lee, "Label-free detection and molecular profiling of exosomes with a nano-plasmonic sensor.," *Nature biotechnology*, vol. 32, pp. 490–5, May 2014. 2

[10] A. A. Yanik, A. E. Cetin, M. Huang, A. Artar, S. H. Mousavi, A. Khanikaev, J. Connor, G. Shvets, and H. Altug, "Ultrasensitive plasmonic fano sensor enables seeing protein monolayers with naked eye," *IEEE Photonic Society 24th Annual Meeting, PHO 2011*, vol. 108, pp. 425–426, July 2011. 2

[11] J. S. Donner, G. Baffou, D. McCloskey, and R. Quidant, "Plasmon-assisted optofluidics," *ACS Nano*, vol. 5, pp. 5457–5462, July 2011. 2

[12] E. Ozbay, "Plasmonics: merging photonics and electronics at nanoscale dimensions.," *Science (New York, N.Y.)*, vol. 311, pp. 189–193, Jan. 2006. 2

[13] D. K. Gramotnev and S. I. Bozhevolnyi, "Plasmonics beyond the diffraction limit," *Nature Photonics*, vol. 4, pp. 83–91, Jan. 2010. 2, 15

[14] S. I. Bozhevolnyi, V. S. Volkov, E. Devaux, J.-Y. Laluet, and T. W. Ebbesen, "Channel plasmon subwavelength waveguide components including interferometers and ring resonators.," *Nature*, vol. 440, pp. 508–511, Mar. 2006. 2

[15] R. F. Oulton, V. J. Sorger, D. A. Genov, D. F. P. Pile, and X. Zhang, "A hybrid plasmonic waveguide for subwavelength confinement and long-range propagation," *Nature Photonics*, vol. 2, pp. 496–500, July 2008. 2

[16] Z. Han, A. Y. Elezzabi, and V. Van, "Experimental realization of subwavelength plasmonic slot waveguides on a silicon platform.," *Optics letters*, vol. 35, pp. 502–504, Feb. 2010. 2

[17] A. Kriesch, S. P. Burgos, D. Ploss, H. Pfeifer, H. A. Atwater, and U. Peschel, "Functional plasmonic nanocircuits with low insertion and propagation losses," *Nano Letters*, vol. 13, pp. 4539–4545, Sept. 2013. 2, 34, 77

[18] G. Veronis and S. Fan, "Modes of subwavelength plasmonic slot waveguides," *Journal of Lightwave Technology*, vol. 25, pp. 2511–2521, Sept. 2007. 2, 22, 27

[19] D. S. Ly-Gagnon, S. E. Kocabas, S. E., and D. A. B. Miller, "Characteristic impedance model for plasmonic metal slot waveguides," *IEEE Journal on Selected Topics in Quantum Electronics*, vol. 14, no. 6, pp. 1473–1478, 2008. 2

[20] S. E. Kocabas, G. Veronis, D. A. B. Miller, and S. Fan, "Modal analysis and coupling in metal-insulator-metal waveguides," *Physical Review B - Condensed Matter and Materials Physics*, vol. 79, p. 035120, Jan. 2009. 2

[21] J. D. Jackson, *Classical Electrodynamics*. Wiley, 1998. 5, 7

[22] C. A. Balanis, *Advanced Engineering Electromagnetics*. Wiley, 2012. 5

[23] D. J. Griffiths, *Introduction to Electrodynamics*. Addison-Wesley, 2012. 5

[24] S. A. Maier, *Plasmonics: Fundamentals and Applications*. Springer, 2007. 9

[25] E. D. Palik, *Handbook of Optical Constants of Solids*. Academic Press, 1985. 10, 13, 25, 30, 39, 59

[26] V. G. Veselago, "the Electrodynamics of Substances With Simultaneously Negative Values of ϵ and μ," *Soviet Physics Uspekhi*, vol. 509, pp. 509–514, Apr. 1968. 10

[27] C. Kittel, *Introduction to Solid State Physics*. Wiley, 2004. 11

[28] A. D. Rakic, A. B. B. Djurisic, J. M. Elazar, and M. L. Majewski, "Optical properties of metallic films for vertical-cavity optoelectronic devices.," *Applied optics*, vol. 37, pp. 5271–5283, Aug. 1998. 13

[29] P. B. Johnson and R. W. Christy, "Optical constants of the noble metals," *Physical Review B*, vol. 6, pp. 4370–4379, Dec. 1972. 13

[30] G. D. Dice, S. Mujumdar, and A. Y. Elezzabi, "Plasmonically enhanced diffusive and subdiffusive metal nanoparticle-dye random laser," *Applied Physics Letters*, vol. 86, pp. 1–3, Mar. 2005. 14

[31] C.-Y. Shih and H.-C. Yeh, "Surface plasmon-enhanced lasing in dye-doped cholesteric liquid crystals," *Optics Express*, vol. 20, p. 20698, Aug. 2012. 14

[32] R. J. Amjad, M. R. Sahar, M. R. Dousti, S. K. Ghoshal, and M. N. a. Jamaludin, "Surface enhanced Raman scattering and plasmon enhanced fluorescence in zinc-tellurite glass.," *Optics express*, vol. 21, pp. 14282–90, June 2013. 14

[33] C. Rosman, J. Prasad, A. Neiser, A. Henkel, J. Edgar, and C. Sönnichsen, "Multiplexed plasmon sensor for rapid label-free analyte detection," *Nano Letters*, vol. 13, pp. 3243–3247, July 2013. 14

[34] G. K. Joshi, K. N. Blodgett, B. B. Muhoberac, M. a. Johnson, K. a. Smith, and R. Sardar, "Ultrasensitive photoreversible molecular sensors of azobenzene- functionalized plasmonic nanoantennas," *Nano Letters*, vol. 14, pp. 532–540, Mar. 2014. 14

[35] J. N. Anker, W. P. Hall, O. Lyandres, N. C. Shah, J. Zhao, and R. P. Van Duyne, "Biosensing with plasmonic nanosensors.," *Nature materials*, vol. 7, pp. 442–453, June 2008. 14

[36] K. L. Kliewer and R. Fuchs, "Collective electronic motion in a metallic slab," *Physical Review*, vol. 153, pp. 498–512, Jan. 1967. 15

[37] E. N. Economou, "Surface plasmons in thin films," *Physical Review*, vol. 182, pp. 539–554, June 1969. 15

[38] D. K. Gramotnev and D. F. P. Pile, "Single-mode subwavelength waveguide with channel plasmon-polaritons in triangular grooves on a metal surface," *Applied Physics Letters*, vol. 85, pp. 6323–6325, Dec. 2004. 15

[39] L. Liu, Z. Han, and S. He, "Novel surface plasmon waveguide for high integration.," *Optics express*, vol. 13, pp. 6645–6650, Aug. 2005. 15

[40] G. Veronis and S. Fan, "Guided subwavelength plasmonic mode supported by a slot in a thin metal film.," *Optics letters*, vol. 30, pp. 3359–3361, Dec. 2005. 15

[41] H. W. H. Lee, G. T. Papadakis, S. P. Burgos, K. Chander, A. Kriesch, R. Pala, U. Peschel, and H. a. Atwater, "Nanoscale conducting oxide plasmonic slot waveguide modulator," *Submitted*, vol. 14, pp. 6463–6468, Nov. 2014. 22

[42] F. Hu, H. Yi, and Z. Zhou, "Wavelength demultiplexing structure based on arrayed plasmonic slot cavities.," *Optics letters*, vol. 36, pp. 1500–1502, Apr. 2011. 22

[43] V. S. Volkov, S. I. Bozhevolnyi, E. Devaux, J. Y. Laluet, and T. W. Ebbesen, "Wavelength selective nanophotonic components utilizing channel plasmon polaritons," *Nano Letters*, vol. 7, pp. 880–884, Apr. 2007. 22

[44] J. A. Dionne, L. A. Sweatlock, H. A. Atwater, and A. Polman, "Plasmon slot waveguides: Towards chip-scale propagation with subwavelength-scale localization," *Physical Review B - Condensed Matter and Materials Physics*, vol. 73, p. 035407, Jan. 2006. 26

[45] W. K. Burns and G. B. Hocker, "End fire coupling between optical fibers and diffused channel waveguides.," *Applied optics*, vol. 16, pp. 2048–2050, Aug. 1977. 33

[46] P. Ginzburg, D. Arbel, and M. Orenstein, "Gap plasmon polariton structure for very efficient microscale-to-nanoscale interfacing.," *Optics letters*, vol. 31, pp. 3288–3290, Nov. 2006. 33

[47] J. Tian, S. Yu, W. Yan, and M. Qiu, "Broadband high-efficiency surface-plasmon-polariton coupler with silicon-metal interface," *Applied Physics Letters*, vol. 95, p. 013504, July 2009. 33

[48] Q. Li, Y. Song, G. Zhou, Y. Su, and M. Qiu, "Asymmetric plasmonic-dielectric coupler with short coupling length, high extinction ratio, and low insertion loss.," *Optics letters*, vol. 35, pp. 3153–5, Oct. 2010. 33

[49] Z. Fang, L. Fan, C. Lin, D. Zhang, A. J. Meixner, and X. Zhu, "Plasmonic coupling of bow tie antennas with Ag nanowire," *Nano Letters*, vol. 11, pp. 1676–1680, Apr. 2011. 34

[50] J. S. Huang, T. Feichtner, P. Biagioni, and B. Hecht, "Impedance matching and emission properties of nanoantennas in an optical nanocircuit," *Nano Letters*, vol. 9, pp. 1897–1902, May 2009. 34

[51] J. Wen, S. Romanov, and U. Peschel, "Excitation of plasmonic gap waveguides by nanoantennas.," *Optics express*, vol. 17, pp. 5925–5932, Mar. 2009. 34

[52] A. Andryieuski, R. Malureanu, G. Biagi, T. Holmgaard, and A. Lavrinenko, "Compact dipole nanoantenna coupler to plasmonic slot waveguide," *Optics Letters*, vol. 37, p. 1124, Mar. 2012. 34, 36, 38

[53] F. Obelleiro, J. M. Taboada, D. M. Solís, and L. Bote, "Directive antenna nanocoupler to plasmonic gap waveguides.," *Optics letters*, vol. 38, pp. 1630–2, May 2013. 34

[54] A. Andryieuski, V. A. Zenin, R. Malureanu, V. S. Volkov, S. I. Bozhevolnyi, and A. V. Lavrinenko, "Direct characterization of plasmonic slot waveguides and nanocouplers," *Nano Letters*, vol. 14, pp. 3925–3929, July 2014. 34, 36

[55] A. Alu and N. Engheta, "Wireless at the nanoscale: Optical interconnects using matched nanoantennas," *Physical Review Letters*, vol. 104, p. 213902, May 2010. 34

[56] T. Liu, Y. Shen, W. Shin, Q. Zhu, S. Fan, and C. Jin, "Dislocated double-layer metal gratings: An efficient unidirectional coupler," *Nano Letters*, vol. 14, pp. 3848–3854, July 2014. 34

[57] F. Lu, F. Xiao, K. Li, and A. Xu, "Ultra-broadband wide-angle unidirectional plasmonic coupler based on joint effects of plasmonic critical angles and subwavelength metallic gratings.," *Optics letters*, vol. 39, pp. 3254–7, June 2014. 34

[58] A. Pors, M. G. Nielsen, T. Bernardin, J.-C. Weeber, and S. I. Bozhevolnyi, "Efficient unidirectional polarization-controlled excitation of surface plasmon polaritons," *Light: Science & Applications*, vol. 3, p. e197, Aug. 2014. 34

[59] X. Li, L. Huang, Q. Tan, B. Bai, and G. Jin, "Integrated plasmonic semi-circular launcher for dielectric-loaded surface plasmon-polariton waveguide.," *Optics express*, vol. 19, pp. 6541–6548, Mar. 2011. 34

[60] I. S. Maksymov and Y. S. Kivshar, "Broadband light coupling to dielectric slot waveguides with tapered plasmonic nanoantennas.," *Optics letters*, vol. 38, pp. 4853–6, Nov. 2013. 34

[61] L. Novotny, "Effective wavelength scaling for optical antennas," *Physical Review Letters*, vol. 98, p. 266802, June 2007. 39

[62] A. Y. Piggott, J. Lu, K. G. Lagoudakis, J. Petykiewicz, T. M. Babinec, and J. Vučković, "Inverse design and demonstration of a compact and broadband on-chip wavelength demultiplexer," *Nature Photonics*, vol. 9, pp. 374–377, May 2015. 47

[63] H. A. Haus, *Waves and Fields in Optoelectronics*. Prentice Hall, 1983. 50

[64] L. F. Solutions, "Using mode expansion monitors," 2015. 56

[65] R. E. Collin, *Field Theory of Guided Waves*. Wiley-IEEE Press, 1990. 56

[66] J. A. Dionne, K. Diest, L. A. Sweatlock, and H. A. Atwater, "PlasMOStor: A metal-oxide-si field effect plasmonic modulator," *Nano Letters*, vol. 9, pp. 897–902, Feb. 2009. 81